Benchmark study using a multi-scale, multi-methodological approach for the petrophysical characterization of reservoir sandstones

Peleg Haruzi[1,2], Regina Katsman[1], Matthias Halisch[3], Nicolas Waldmann[1], and Baruch Spiro[1,4]

[1] The Dr. Moses Strauss Department of Marine Geosciences, Faculty of Natural Sciences, The University of Haifa, Haifa, Mount Carmel 3498838, Israel

[2]Agrosphere Institute, IBG-3, Institute of Bio- and Geosciences, Forschungszentrum Jülich GmbH, Germany

[3] Leibniz Institute for Applied Geophysics, Dept. 5 – Petrophysics & Borehole Geophysics, Stilleweg 2, D-30655 Hannover, Germany

[4] Department of Earth Sciences, Natural History Museum, Cromwell Road, London SW7 5BD, UK

Correspondence to: Regina Katsman (rkatsman@univ.haifa.ac.il)

Matthias Halisch (Matthias.Halisch@leibniz-liag.de)

Keywords: multi-methodological approach, permeability, petrography, petrophysics, 3D imaging, pore-scale modelling, upscaling, semivariogram modelling, benchmark study.

Abstract

This paper presents a detailed description and evaluation of a multi-methodological petrophysical approach for the comprehensive multiscale characterization of reservoir sandstones. The suggested methodology enables the identification of Darcy-scale permeability links to an extensive set of geometrical, textural and topological rock descriptors quantified at the pore scale. This approach is applied to the study of samples from three consecutive sandstone layers of Lower Cretaceous age in northern Israel. These layers differ in features observed at the outcrop, hand specimen, petrographic microscope and micro-CT scales. Specifically, laboratory porosity and permeability measurements of several centimetre-sized samples show low variability in the quartz arenite (top and bottom) layers but high variability in the quartz wacke (middle) layer. The magnitudes of this variability are also confirmed by representative volume sizes and by semivariogram analyses conducted on micro-CT-imaged 3D pore geometries. Two scales of porosity variability are revealed by applying a semivariogram analysis to quartz arenite sandstone of the top layer: the pore size scale of ~100 μm, and ~1.6 mm scale due to the occurrence of high- and low-porosity horizontal bands occluded by Fe oxide cementation. This millimetre-scale variability is found to control the laboratory-measured macroscopic rock permeability. More heterogeneous pore structures were revealed in the quartz wacke sandstone of the intermediate layer, which comprises an internal spatial irregularity at the different scales: at the pore size scale and at the larger scale of porous “lenses” originated in presence of patchy clay deposition. Quartz arenite sandstone of the bottom layer shows stationarity and isotropy in the investigated domain revealing porosity variability at a ~0.1 mm scale, which is associated with the average size of pore cross-section. Good agreement between the permeability upscaled from the pore-scale modelling and the estimates based on laboratory measurements is shown for the quartz arenite layers. The proposed multi-methodological approach leads to an accurate petrophysical characterization of reservoir sandstones with broad ranges of textural, topological and mineralogical characteristics and is particularly applicable for describing anisotropy at various rock scales. The results of this study also contribute to the geological interpretation of the studied stratigraphic units.

1. Introduction

Permeability is an effective property of a reservoir rock that varies enormously over a wide range of rock length scales, attributed to a hierarchy of dominant sedimentary depositional features (Norris and Lewis, 1991; Nordahl and Ringrose, 2008; Ringrose and Bentley, 2015). Permeability should thus be properly upscaled through the following sequence of scales (Nordahl and Ringrose, 2008; Ringrose and Bentley, 2015 and references therein): (1) from the pore scale (the micro scale, typically microns to millimetres) to the representative elementary volume of a single lamina (the macro scale, typically millimetres to centimetres, e.g., Wildenschild and Sheppard, 2013; Andrä et al., 2013b ; Bogdanov et al., 2011; Narsilio et al., 2009); (2) to the scale of geological heterogeneity, e.g., the scale of a stratigraphic column (decimetres to decametres, e.g., Jackson et al. 2003; Nordahl et al. 2005); and (3) to the field scale or the scale of an entire reservoir or aquifer (hundreds of metres to kilometres) (Haldorsen and Lake 1984; Rustad et al., 2008). Pore scale imaging and modelling enable us to relate macroscopic permeability to basic microscopic rock descriptors (Kalaydjian, 1990; Whitaker, 1986; Cerepi et al., 2002; Haoguang et al., 2014; Nelson, 2009). Therefore, the first stage in the above sequence is crucial for successful upscaling to the final reservoir scale permeability.

Over the past few decades, 3D pore scale imaging and flow simulations (Bogdanov et al., 2012; Blunt et al., 2013; Cnudde and Boone, 2013; Wildenschild and Sheppard, 2013; Halisch, 2013a) have started to serve as a reliable method for rock characterization. The advantages of these techniques are their non-destructive character and their capability to provide reliable information about the real pore-space structure and topology of rocks that is impossible to obtain using the conventional experimental methods (e.g., Arns et al., 2007; Knackstedt et al., 2010; Blunt et al., 2013). However, despite its importance, the upscaling from the pore scale is sometimes omitted; as a result, effective petrophysical rock characteristics (e.g., porosity, surface area, and permeability) are often evaluated at the macro scale through only conventional laboratory experiments, which often suffer from errors due to local heterogeneities, anisotropy, or an insufficient number of samples (e.g., Meyer, 2002; Halisch, 2013a).

Digital 3D micro scale core analysis should also become a necessary technique for rocks that are difficult to characterize due to various reasons (e.g., for tight sandstones, Liu et al., 2017; Du et al., 2018; Munawar et al., 2018; Zhang et al., 2019), or for those with inhomogeneous or anisotropic pore space (e.g., Meyer, 2002; Farrel et al., 2014). Preferential fluid flow pathways are inherently connected to rock microstructure, formed by depositional sedimentary structures such as pore shapes and their preferential orientation (Sato et al., 2019) or lamination (Lewis et al., 1988). Those can be modified with time by dissolution of grains, by grain rearrangement and pore collapse (Halisch et al., 2009; Clavaud et al., 2008), by cementation (Louis et al., 2005), or by deformation structures (fractures). The later may drastically alter the host rock depositional porosity pattern and create new permeability pathways (Zhu et al., 2002; Farrel et al., 2014).

The present paper provides a detailed description and evaluation of a multi-methodological petrophysical approach for the comprehensive multiscale characterization of reservoir sandstones. The proposed approach includes petrography, gas porosimetry and permeametry, mercury intrusion porosimetry, 3D imaging and image analysis, semivariogram analysis and flow modelling at the pore-scale. The suggested computational workflow enables the identification of Darcy scale permeability links to an extensive set of geometrical, textural and topological rock descriptors, quantified at the pore scale by deterministic methods. Ultimately, this approach is applied to the study of three different consecutive sandstone layers of Lower Cretaceous age in northern Israel.

The approach presented herein is especially important for the detection of anisotropy and the identification of its origin at various rock scales. The multi-methodological validation procedure is significant for properly upscaling permeability from the micro scale to the macro scale (Ringrose and Bentley, 2015). This validation, thereby, allows an accurate petrophysical analysis of reservoir sandstones with broad ranges of textural and topological characteristics. The findings contribute also to the current geological knowledge regarding non-marine sandstones of Lower Cretaceous age (e.g., Akinlotan, 2016; 2017; 2018; Li et al., 2016; Ferreira et al., 2016) and specifically regarding the studied stratigraphic unit.

2. Geological setting

The study is based on samples collected from a steep outcrop at Wadi E'Shatr near Ein Kinya on the southern slopes of Mt. Hermon (Figure 1). The outcrop consists of sandstones from the Lower Cretaceous Hatira Formation (Sneh and Weinberger, 2003). This formation (Fm.) acts as a reservoir rock for hydrocarbons in Israel (Figure 1a), both onshore, namely, Heletz (Grader and Reiss, 1958; Grader, 1959; Shenhav, 1971, Calvo, 1992; Calvo et al., 2011), and offshore, namely, Yam Yafo (Gardosh and Tannenbaum, 2014; Cohen, 1971; Cohen, 1983;).

The Hatira Fm. is the lower part of the Kurnub Group of Lower Cretaceous (Neocomian – Barremian) age. The Hatira Fm. nomenclature used in Israel and Jordan is equivalent to Grès de Base in Lebanon (Massaad, 1976). This formation occurs in Israel in outcrops from the Eilat area along the rift valley, in the central Negev, and in the northernmost outcrops on Mount Hermon; it forms part of a large Palaeozoic – Mesozoic platform and continental margin deposits in northeastern Africa and Arabia. The Hatira Fm. consists of siliciclastic units, typically dominated by quartz-rich sandstones (Kolodner et al., 2009 and references therein). The underlying Palaeozoic sandstones cover large areas in North Africa and Arabia from Morocco to Oman; these sandstones overlie a Precambrian basement affected by Neoproterozoic (pan African) orogenesis (Garfunkel, 1988, 1999; Avigad et al., 2003, 2005). The lower Palaeozoic sandstones in Israel and Jordan originated from the erosion of that Neoproterozoic basement, the Arabian-Nubian Shield, with contributions from older sources. These lower Palaeozoic sandstones (Cambrian and Ordovician) are described as first-cycle sediments (Weissbrod and Nachmias, 1986; Amireh, 1997; Avigad et al., 2005). Exposures of the Hatira Fm. in the Central Negev, the Arava Valley, Eilat and Sinai were originally defined as the Wadi (Kurnub) Hatira Sandstone (Shaw, 1947). The largely siliciclastic section of the Hatira Fm. is intercalated with carbonates and shales representing marine ingressions that increase towards the north (Weissbrod, 2002).

The Lower Cretaceous sandstones of the Kurnub Group are described as super mature, cross-bedded, medium- to fine-grained, moderately sorted to well-sorted quartz arenites with a high zircon-tourmaline-rutil (ZTR) index (for more details, see Kolodner, 2009). Earlier observations indicate the relatively scarce occurrence of siltstones and claystones compared to sandstones (Massaad, 1976; Abed, 1982; Amireh, 1997). These Lower Cretaceous sandstones are mainly the recycled products of older siliciclastic rocks throughout the Phanerozoic; the sand was first eroded from the surface of the pan African orogeny ca. 400 Ma prior to its deposition in the Lower Cretaceous sediments (Kolodner et al., 2009).

The Mount Hermon block was located at the southern border of the Tethys Ocean during the Early Cretaceous (Bachman and Hirsch, 2006). A paleo-geographical reconstruction indicates that the sandy Hatira Fm. (Figure 1) was deposited in a large basin, which included both terrestrial and coastal environments such as swamps and lagoons (Sneh and Weinberger, 2003). The Hermon block, located next to the Dead Sea Transform, was rapidly uplifted during the Neogene (Shimron, 1998). The area is marked by intense erosion, which resulted in extensive outcrops such as those near Ein Kinya on the southeastern side of Wadi E'Shatr.

The Kurnub Group in the study area (Figure 1b, d) consists of a volcanic sequence at its base that is overlain with an angular uncomformity by sandstone and clay layers of the Hatira Fm.; the upper unit consists of limestone, marl and chalk – the Nabi Said Fm. (Sneh and Weinberger, 2003). At the section of Saltzman (1968), which is approximately 100 m SW of the sampling area of the present study, the 58 m thick variegated sandstone is interbedded with layers of clay and clay-marl. The sandy component is white-yellow-brown/red and consists of largely angular, poorly sorted, fine- to coarse-grained quartz sand. Individual sandstone layers are cemented by Fe oxide (Fe-ox). The outcrops show lenticular benches 0.2 m -1.0 m thick. The clay-rich interlayers are grey and normally siltic and brittle. Locally, these layers contain lignite. The outcrop investigated and the specific beds sampled in the present study are shown in Figure 1c.

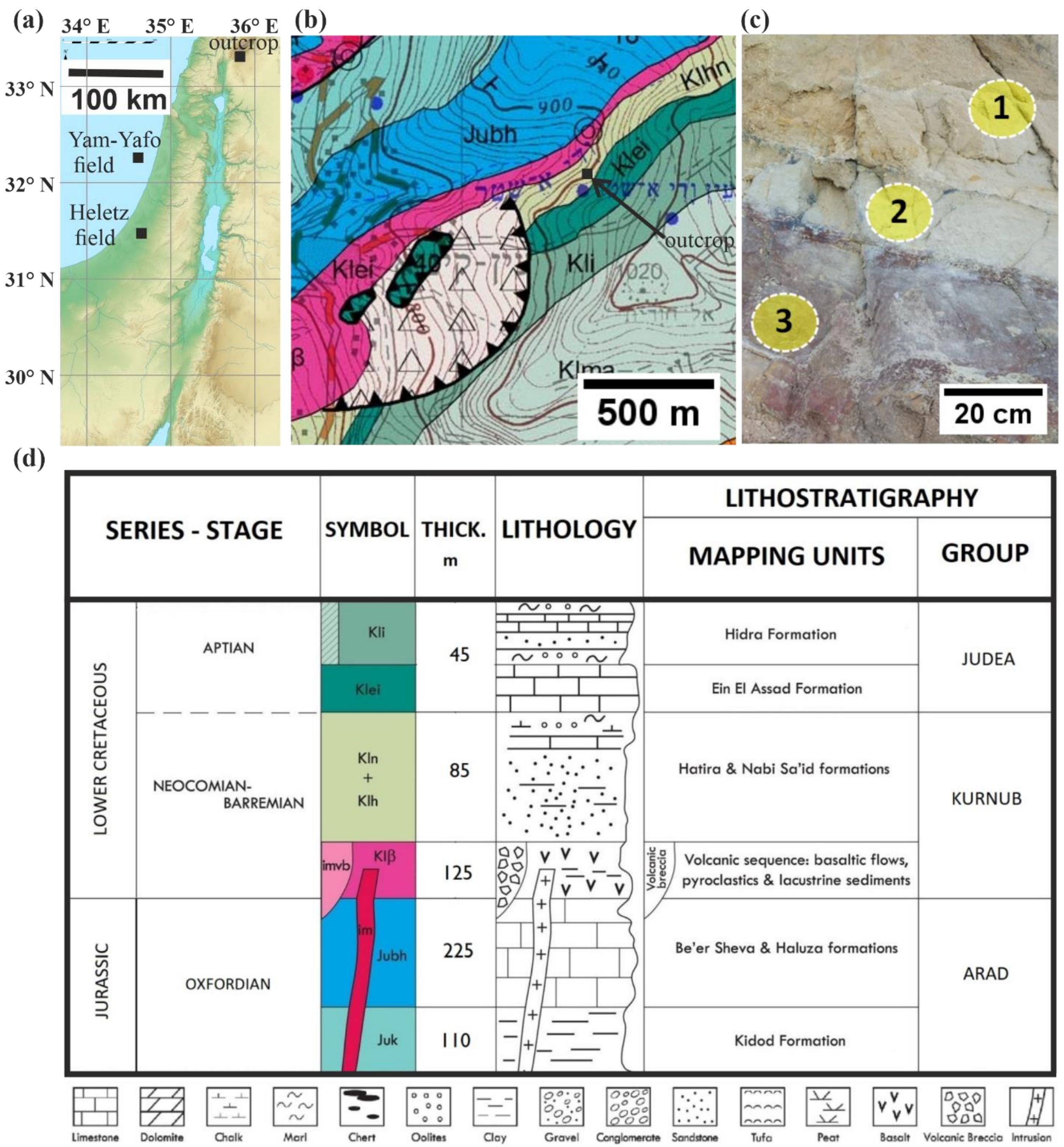

Figure 1: *Geographical and geological settings. (a) Schematic relief map of Israel (modified from www.mapsland.com). (b) Geological map of Ein Kinya. The Hatira Fm. sandstone and the overlying limestone and marl of the Nabi Said Fm.*

are marked as Klhn (map is adopted from Sneh and Weinberger, 2014). (c) Outcrop of the Lower Cretaceous *Hatira Fm. sandstones (Klhn) at Ein Kinya. The studied sandstone layers have distinct colours: yellow-brown (1), grey-green (2), and red-purple (3). (d) Stratigraphic table of the geological map (modified from Sneh and Weinberger, 2014).*

3. Methods

3.1. Sample description

Samples were extracted from three consecutive layers of different colours from a stratigraphic sequence (Figs. 1c, 1d). The lower layer (3) is ~1.5 m thick and consists of sandstone that is light (pale) red-purple in colour with undulating bedding planes between the sub-layers. The middle layer (2) is composed of grey – green shaly sandstone that is 20 cm thick with dark horizons at the bottom and top. The upper layer (1) comprises 1.5 m thick homogenous brown-yellow sandstone. Large sample blocks of ~10÷20 cm size were collected from these three layers, and the directions perpendicular to the bedding planes (defined as the z-directions in our study) were noted. Subsequently, in the laboratory, smaller sub-samples (described below) were prepared from these large samples for textural observations and various analytical measurements and computations. In total, 7 sub-samples from the top layer, 8 sub-samples from the middle layer and 4 sub-samples from the bottom layer were investigated in the laboratory (Table 2).

3.2. Laboratory and computational methods for rock characterization

The integrated analytical programme designed for this study includes the following laboratory measurements and computations conducted at different scales (from the micro scale reflecting the scale of individual pores and grains to the core scale reflecting the scale of the laminas at the outcrop) (Table 1). Specimens ~5-7 cm in size were investigated by petrographic and petrophysical lab methods. Sub-samples ~1 cm in size were retrieved from the aforementioned plugs for investigation by 3D imaging, digital image analysis and simulation techniques (described in more detail below).

Petrographic and petrophysical analysis (#1-7 in Table 1) have been conducted following the RP40 guidelines (*Recommended Practices for Core Analysis, API, 1998*), giving detailed information on theory, advantages and drawbacks of each method. Extended computational workflow (#8 in Table 1) combines several methods that may contain some variability in their application for the rock characterization. Those are described in more detail below.

Table 1. *Laboratory methods employed and petrophysical characteristics determined from these methods*

Method	**Determined petrophysical characteristics**
1. Scanning electron microscopy (SEM)	Mineral abundance, grain surface characterization of matrix and cementation
2. Grain size analysis (Laser diffraction)	Grain size distribution (*GSD*)
3. X-ray diffraction (XRD)	Mineral components
4. Nitrogen gas porosimetry	Porosity (ϕ)
5. Steady state permeametry	Permeability (1D) (κ)
6. Mercury intrusion porosimetry (MIP)	Pore throat size distribution (*PTSD*), specific surface area (*SSA*), characteristic length (l_c), pore throat length of maximal conductance (l_{max}), permeability (κ)
7. Optical microscopy Plane-parallelized (PPL) and cross-parallelized (XPL) and reflected-light (RL) microscopy, binocular (BINO).	Mineral abundance, grain surface characterization, cementation
8. Extended computational workflow:	
Digital image analysis (DIA)	Porosity (ϕ), pore specific surface area (*PSA*), tortuosity (τ), pore size distribution (*PSD*), connectivity index (*CI*), micro-CT predicted porosity from MIP
Semivariogram analyses	Range of spatial correlation of pore structures
Fluid flow modelling	Permeability tensor ($\bar{\bar{\kappa}}$), tortuosity (τ)

Petrographic descriptions of rock compositions and textures at the micro scale, notably those of the fine fraction, were performed using scanning electron microscopy (*JCM-6000 Bench Top SEM device*; e.g., Krinsley et al., 2005) using both backscatter and secondary electron modes.

Thin-section optical microscopy (*Olympus BX53 device*, e.g., MacKenzie et al., 2017) was used to estimate the mineral abundance and surface features of the grains, and the mineralogical and textural features of matrix and cement. Grain size distributions were determined by a laser diffraction particle size analyser (*LS*

13 320; e.g., Wang et al., 2013). X-ray diffraction (*Miniflex 600 device by Rigaku*; e.g., Asakawa et al., 2020) was applied to powdered samples to determine their mineralogical composition.

Effective porosity and permeability were evaluated on dried cylindrical samples (2.5 cm in diameter and 5-7 cm in length). Effective porosity (ϕ) was measured using a steady-state nitrogen gas porosimeter produced by Vinci Technologies (*HEP-E, Vinci Technologies*; e.g. Viswanathan et al., 2018). Absolute permeability (κ) was measured by using a steady-state nitrogen gas permeameter (*GPE, Vinci Technologies*; e.g., Tidwell et al., 1999).

Mercury intrusion porosimetry (*Micromeritics AutoPore IV 9505*, which considers pore throats larger than 0.006 μm; e.g., Giesche, 2006) was applied to dried cylindrical samples ~1 cm^3 in size to evaluate the following parameters (Table 1):

- Pore throat size distribution (*PTSD*, Lenormand, 2003).
- Specific surface area (*SSA*): the pore surface to bulk sample volume (Rootare and Prenzlow, 1967; Giesche, 2006).
- Characteristic length (l_c): the largest pore throat width (obtained from the increasing intrusion pressure) at which mercury forms a connected cluster (Katz and Thompson, 1987).
- Pore throat length of maximal conductance (l_{max}): defines a threshold for the pore throat size l at which all connected paths composed of $l \geq l_{max}$ contribute significantly to the hydraulic conductance, whereas those with $l < l_{max}$ may completely be ignored (Katz and Thompson, 1987).
- Permeability (Katz and Thompson, 1987):

$$\kappa = \frac{1}{89} l_{max}^2 \frac{l_{max}}{l_c} \phi S(l_{max}) \quad (1)$$

where $S(l_{max})$ is the fraction of connected pore space that is composed of pore throat widths of size l_{max} and larger. This approach (Katz and Thompson, 1987), which was derived from percolation theory (Ambegaokar et al., 1971), is applicable for sandstones with a broad distribution of local conductances with short-range correlations only.

An extended computational workflow (similar to the procedure presented by Boek and Venturoli, 2010; Andrä et al., 2013a,b) (Figure 2) serves as one of the main methodologies in our study to upscale permeability.

It includes 3D micro-CT imaging of porous samples, digital image processing and segmentation, statistical analyses for the determination of representative elementary volumes, and pore-scale flow modelling through the 3D pore geometry of the rock. First, cylindrical subsamples 4-8 mm in diameter and 5-10 mm in length were retrieved from the larger samples studied in the laboratory and were scanned non-destructively (Figure 2b) by using a *Nanotom* 180 S micro-CT device (*GE Sensing & Inspection Technologies*, *phoenix|X-ray product line*, Brunke et al., 2008). The achieved voxel size of the data sets was 2.5 µm or 5 µm (isotropic), suitable for imaging pore throats that effectively contribute to the flow in the studied type of sandstone (e.g., Nelson, 2009). Afterwards, all data sets were filtered for de-noising, X-ray artefact removal and edge enhancement (Figure 2c). The post-processed images scanned with 2.5 µm resolution had an edge length of 1180 voxels or 2950 µm. Image artefacts were processed as described by Wildenschild and Sheppard (2013). Beam hardening artefacts were removed by applying the best-fit quadratic surface algorithm (Khan et al., 2016) to each reconstructed 2D slice of the image. Ring artefact reduction and image smoothing (with preservation of sharp edge contrasts) were performed using a non-local means filter (Schlüter, 2014). Segmentation was performed to convert the grey-scale images obtained after image filtering into binary images to distinguish between voids and solid phases (Figure 2c). The local segmentation approach, which considers the spatial dependence of the intensity for the determination of a voxel phase, was used in addition to a histogram-based approach (Iassonov et al., 2009; Schlüter et al., 2014). Two-phase segmentation was performed by the converging active contours algorithm (Sheppard et al., 2004), a combination of a watershed (Vincent et al., 1991) with an active contour algorithm (Kass et al., 1988).

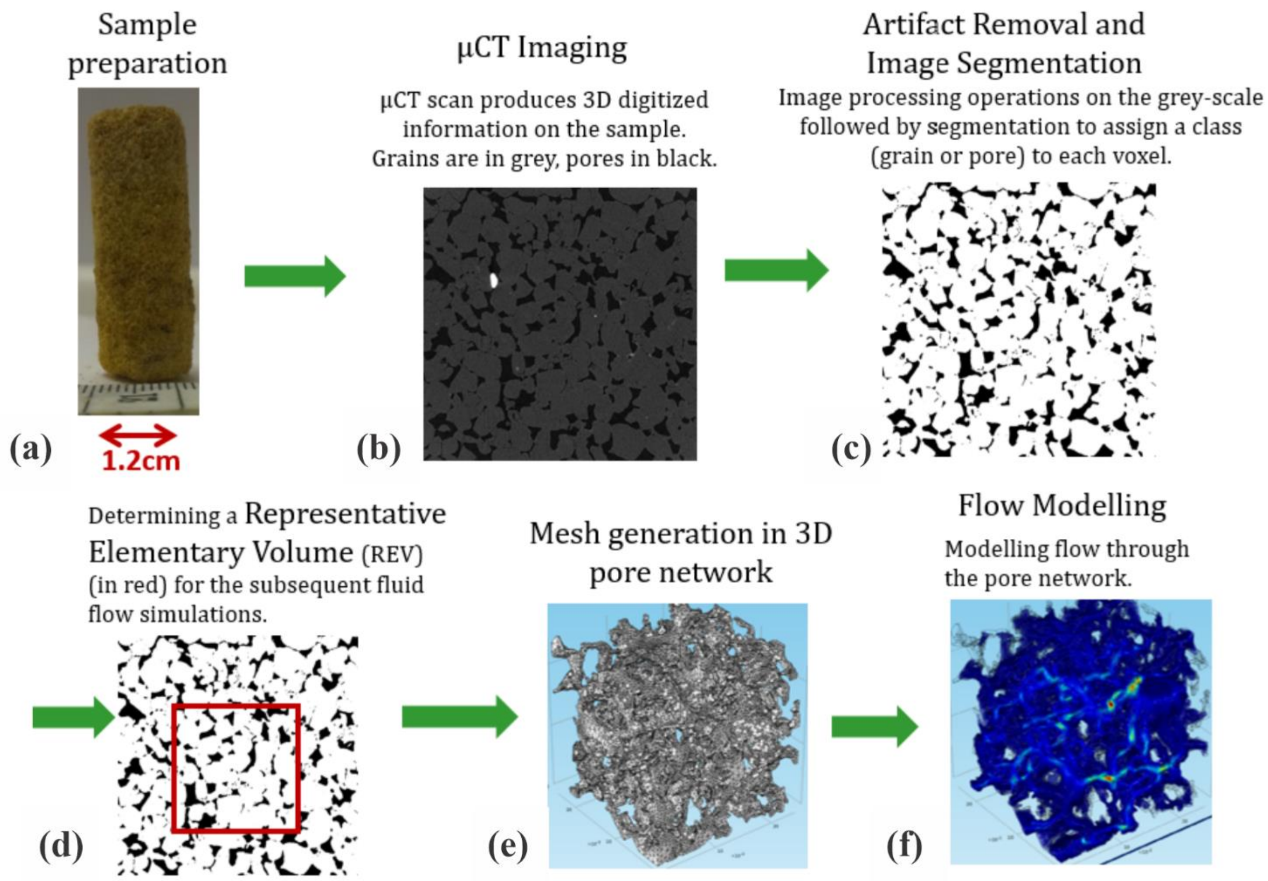

***Figure 2:** Extended computational workflow. See text for more details. Images **(e)** and **(f)** are adopted from Bogdanov et al. (2012).*

Simulations involving the real geometry of an imaged rock are computationally power and time consuming. Therefore, the determination of a representative elementary volume (REV) is required (Figure 2d), assuming that porous media are homogeneous at REV dimensions (Bear, 2013). A REV is required in the current study to perform fluid flow simulations. Porosity, a basic macroscopic structural property of porous media, is used here for the estimation of an REV (Bear, 2013; Halisch, 2013a; Tatomir et al., 2016) based on its correlation with permeability (Kozeny, 1927; Carman, 1937) (see discussion on this issue in the Discussion Sect.).

Two approaches were used in this study to estimate the REV (Halisch, 2013a,b). In the "classic" approach, the REV is attained when porosity fluctuations in the sub-volumes that grow isotropically in three orthogonal directions become sufficiently small (Bear, 2013). Practically, a large number of randomly distributed cubes were analysed through the entire 3D sample (with a 1180 voxel edge length in our case) for their image porosity (IP). The chosen initial cube size (with an edge length of 10 pixels in our case) was increased by 10-100 voxels. The REV size was specified when agreements between the mean and median IP values as well as saturation in the IP fluctuations were attained. The results of the REV estimation by this classic approach can be found in Appendix A.

A more advanced "directional" REV approach can capture porosity changes in a specific direction caused by microscopic structural features, such as grain packing, cracks, and textural effects (Halisch, 2013b). The IP is calculated slice by slice across the segmented image in each orthogonal direction.

Semivariogram analysis was also conducted to estimate the REV. Semivariogram (Cressie, 1985) defines the relation between a spatially varying property (porosity in our case) and a lag distance (a Cartesian distance between the points in the studied domain). The semivariogram value increases when the values of the studied parameter become more dissimilar. Semivariogram, $\gamma(h)$, is based on the difference in values of the studied property between all combinations of pairs of data points, x_i and y_i, in the studied domain and is defined by:

$$\gamma(h) = \frac{1}{2N(h)} \sum_{i=1}^{N(h)} (x_i - y_i)^2 \quad (2),$$

where $N(h)$ is the number of pairs, and h is the lag distance. A semivariogram describing a single variability structure is characterized by a sill (a plateau) in which γ corresponds to the total variability of the sample, and by the range (of correlation) in h at which γ reaches the sill value (usually ~95 % of the sill value). Due to the spatial continuity of the CT dataset, a lag increment of a voxel size set by the CT acquisition resolution, was chosen for calculation of the semivariogram, thus producing a large amount of data point pairs at each lag to get a significant mean (Ploner, 1999). A non-zero intercept in the semivariogram (nugget effect) may exist due to variability at lengths smaller than the lag distance and due to noisy data. For CT data, natural variations below the fixed resolution limit are invisible for the variography analysis. Therefore, in CT data the nugget effect may be observed only due to measurement error inherent to measuring devices. In a case they are small, the semivariogram will approximately have a zero intercept.

There are several analytical models that fit the semivariograms. In this study we use three of them (for more information see Cressie, 1985).

Gaussian: $\gamma(h) = C\left[1 - \exp\left(-3(\frac{h}{a})^2\right)\right]$ (3)

Spherical: $\gamma(h) = C\left[\frac{3}{2}\frac{h}{a} - \frac{1}{2}\left(\frac{h}{a}\right)^3\right]$ for $h<a$, C else. (4)

Hole-effect: $\gamma(h) = C\left[1 - cos\left(\frac{h}{a}\pi\right)\right]$ (5)

where C is the calibrated sill and a is a calibrated parameter.

Multiple sills may be associated with different variability structures, which are characteristic, for instance, for the different scales. Nested sills are modelled as a linear combination of the single models:

Nested sills: $\gamma(h) = \sum_{i=1}^{n} C_i\gamma_i(h)$, $0<C$ (6)

where C_i is the contribution of a single sill.

z-direction of CT specimen used in this analysis is perpendicular to the natural layering of the sandstone identified in the outcrop and in the petrographic observations. x- and y- orthogonal directions lie in the horizontal plane, with an azimuth chosen randomly. The application of the semivariogram analysis using all data points (the voxels) distributed at multiple 3D sub-volume domains, is computationally intensive as the typical CT dataset includes 10^9 points and more. To allow faster semivariogram calculations, we slice the volume by cross-sections with a voxel size distance between them in each direction and evaluate the porosity at each cross-section, which produces a one-dimensional porosity profile. This results in histograms (the population of cross-sections porosity) that differ in each direction and also from those in the original 3D dataset. Therefore, for each direction a semivariogram model is independently calculated and modelled. In case when the variable is identified with a spatial systematic trend, the mean value will not to be independent of location (considered as a non-stationarity) that disconsiders the representativeness of the sample. When such a trend is identified, it should be modelled and removed from the property dataset, to remain with residuals. Next, a common practice is to calculate the semivariogram to a standardized histogram of the data to have a sill of 1 (Gringarten and Deutsch, 2001), which is achieved by z-score transformation (a normal score transform) of the residual porosity histograms. For evaluation of representative lengths, when along some direction the variability changes merely with an increasing lag distance, a sill (in a nested model) is calibrated and the resulting calibrated range represents a length associated with a natural spatial structure in the sample. When a sill is calibrated similarly to the complete variability (sill~1) in the sample, the calibrated range is defined as a representative length in the studied direction. The experimental and modelled (Eqs.3-6) semivariograms were calculated in this study using dedicated MATLAB packages (Schwanghart, 2020a,b).

Further, the representative binary 3D image (REV) of the pore space was spatially discretised by tetrahedrals with *Materialize software (Belgium)* (Figure 2e). This step is required for importing the REV into the FEM-based modelling software (*Comsol Multiphysics simulation environment*, v5.2a). Stokes flow (Re << 1) is simulated (Table 1) in the pore network (Figure 2f) by the following equations (e.g., Narsilio et al., 2009; Bogdanov et al., 2011):

Stokes equation: $$-\nabla p + \mu \nabla^2 \bar{u} = 0 \quad (7)$$

Continuity equation: $$\nabla \cdot \bar{u} = 0 \quad (8)$$

where ∇p is the local pressure gradient, $\bar{u}$ is the local velocity vector in the pore space and μ is the dynamic fluid viscosity. Fixed pressures (*p=const*) were specified at the inlet and outlet boundaries of the fluid domain with a constant pressure gradient of 2.424 Pa/mm over the domain prescribed in all the simulations for consistency. At the internal pore walls and at the lateral domain boundaries, no-slip boundary conditions ($\bar{u} = 0$) were imposed (e.g., Guibert et al., 2016). These also simulate the flow setup in a steady-state experimental permeameter (e.g., Renard et al., 2001). The macroscopic fluid velocity $< \bar{v} >$ was evaluated by volumetrically averaging the local microscopic velocity field (e.g., Narsilio, 2009; Guibert et al., 2016). Then, from the average macroscopic velocity vectors v_i^j in three orthogonal *i*-directions corresponding to the pressure gradients ∇p_j imposed in *j*-directions, the full 3D second-rank upscaled permeability tensor $\bar{\bar{\kappa}}$ can be found:

$$\begin{pmatrix} v_x^x & v_x^y & v_x^z \\ v_y^x & v_y^y & v_y^z \\ v_z^x & v_z^y & v_z^z \end{pmatrix} = -\frac{1}{\mu\phi} \begin{pmatrix} \kappa_{xx} & \kappa_{xy} & \kappa_{xz} \\ \kappa_{yx} & \kappa_{yy} & \kappa_{yz} \\ \kappa_{zx} & \kappa_{zy} & \kappa_{zz} \end{pmatrix} \begin{pmatrix} \nabla p_x & 0 & 0 \\ 0 & \nabla p_y & 0 \\ 0 & 0 & \nabla p_z \end{pmatrix} \quad (9)$$

The permeability tensor is symmetrized by:

$$\bar{\bar{\kappa}}_{sym} = \frac{1}{2}(\bar{\bar{\kappa}} + \bar{\bar{\kappa}}^T) \quad (10)$$

Tortuosity (τ; Bear, 2013; Boudreau, 1996) was calculated separately in the x-, y- and z-directions in the meshed domain using the particle tracing tool of *Comsol Multiphysics software* (an additional method for deriving τ is presented later in this section).

3D image analysis (Table 1) was conducted on a high-quality, fully segmented micro-CT image (edge length of 2950 µm scanned at a 2.5 µm voxel size). Non-connected void clusters in the binary specimen were labelled and then separated into objects (single pores and grains) by using a distance map followed by the application of a watershed algorithm (e.g., Brabant et al., 2011; Dullien, 2012). Image analysis operations were assisted by *Fiji-ImageJ software* (Schindelin et al., 2012) and by the *MorphoLibJ plug-in* (Legland et al., 2014). The following geometrical descriptors were derived from the segmented image limited by the image resolution of 2.5 µm (Table 1):

- micro-CT image porosity (*IP*);
- Pore specific surface area (*PSA* – surface to pore volume);
- Tortuosity: evaluated in the x-, y- and z-directions by finding the average of multiple shortest paths through the main pore network using the fast marching method (Sethian, 1996) implemented using an accurate fast marching plug-in in MATLAB.
- Pore size distribution (*PSD*): obtained by a Feret maximum calliper (Schmitt et al., 2016).
- Euler characteristic (χ) - a topological invariant (Wildenschild and Sheppard, 2013; Vogel, 2002) that describes the structure of a topological space (see Supplementary material for more detail). Since the number of pore connections depends on the number of grains, it is essential to normalize χ (Scholz et al., 2012) to compare the connectivity among three samples that have the same dimensions but different grain sizes.
- Connectivity index (*CI*): computed by dividing the absolute value of the Euler characteristic ($|\chi|$) by the number of grains in the specimen (*N*, determined by image analysis), $CI = |\chi|/N$.

Table 1 allows conducting a comparison between the characteristics derived by the different methods at the different scales of investigation (similarly to Table 1 in Tatomir et al. (2016) that focuses on the similar rock).

Additionally, we propose a simple and new method to estimate the image porosity at a given resolution. Multiplication of the mercury effective saturation at the capillary pressure corresponding to the micro-CT resolution (e.g., 2.5 μm) by the porosity of the same sample measured by a gas porosimeter yields the *micro-CT-predicted image porosity from MIP* at the given resolution limit (Table 1).

4. Results

4.1. Petrographic and petrophysical rock characteristics

Three types of sandstone rocks were characterized by techniques 1-8 listed in Table 1. The results are presented in Figures 3-8 and summarized in Table 2.

Sandstone S1: The top unit layer with a thickness of ~1.5 m (Figure 1c) consists of yellow-brown sandstone (Figure 3a), which is moderately consolidated. The sandstone is a mature quartz arenite (following Pettijohn et al., 1987) with minor Fe-ox, feldspar and heavy minerals (e.g., rutile and zirconium). The grain size distribution has a mean of ~325 µm (Figure 6a, Table 2). The grains are moderately sorted (according to the classification of Folk and Ward, 1957) and sub-rounded to well-rounded with local thick (millimetre-scale), relatively dark envelopes (Figure 3b). The sandstone consists of alternating millimetre-scale layers of large and small sand grains. Secondary silt (~ 45 µm) and clay (~0.95 µm) populations are detected in the grain size distribution (Figure 6). X-ray diffraction detected a small amount of kaolinite. The Fe-ox grain-coating and meniscus-bridging cement is composed of overgrown flakes aggregated into structures ~10 µm in size (Figure 3c-3f). Mn oxide is also evident but is scarce (Figure 3e).

The pore network is dominated by primary inter-granular well-interconnected macro porosity (Figure 3b). However, sealed and unsealed cracks in grains are also observed. Higher Fe-ox cementation at the millimetre scale on horizontal planes is recognized (Figure 3a). In addition, smaller voids between Fe-ox aggregates and flakes occur at the micrometre scale and smaller (Figure 3d-f).

The pore throat size analysis conducted with MIP shows that 82 % of the pore volume is composed of macro pores (>10 µm) following a log-normal distribution with a peak at 44 µm (Figure 7a). The characteristic length, i.e., the largest pore throat length at which mercury forms a connected cluster, is $l_c = 42.9$ µm (Figure 7b), and the pore throat length of maximal conductance is $l_{max} = 34.7$ µm (Appendix B, Figure B1). The porosity evaluated by laboratory gas porosimetry varies in the range of 26-29 % for 7 different samples of S1 (Figure 8). Multiplying the mercury effective saturation (85.8 %) at the micro-CT resolution (2.5 µm) (Figure 7a, red dashed line) by the porosity of the same sample measured by gas porosimetry (27.3 %) yields a micro-CT-predicted image porosity of 23.5 % at a resolution limit of 2.5 µm (Table 2).

The permeability evaluated by a laboratory gas permeameter has averages of 350 mD (range of 130-500 mD) for 5 samples measured perpendicular to the depositional plane (z-direction) and 640 mD for 2 samples measured parallel to the depositional plane (x- and y-directions) (Figure 8). MIP measurement (Katz and Thompson, 1987) yields a permeability (see Sect. 3.2) of 330 mD (Table 2).

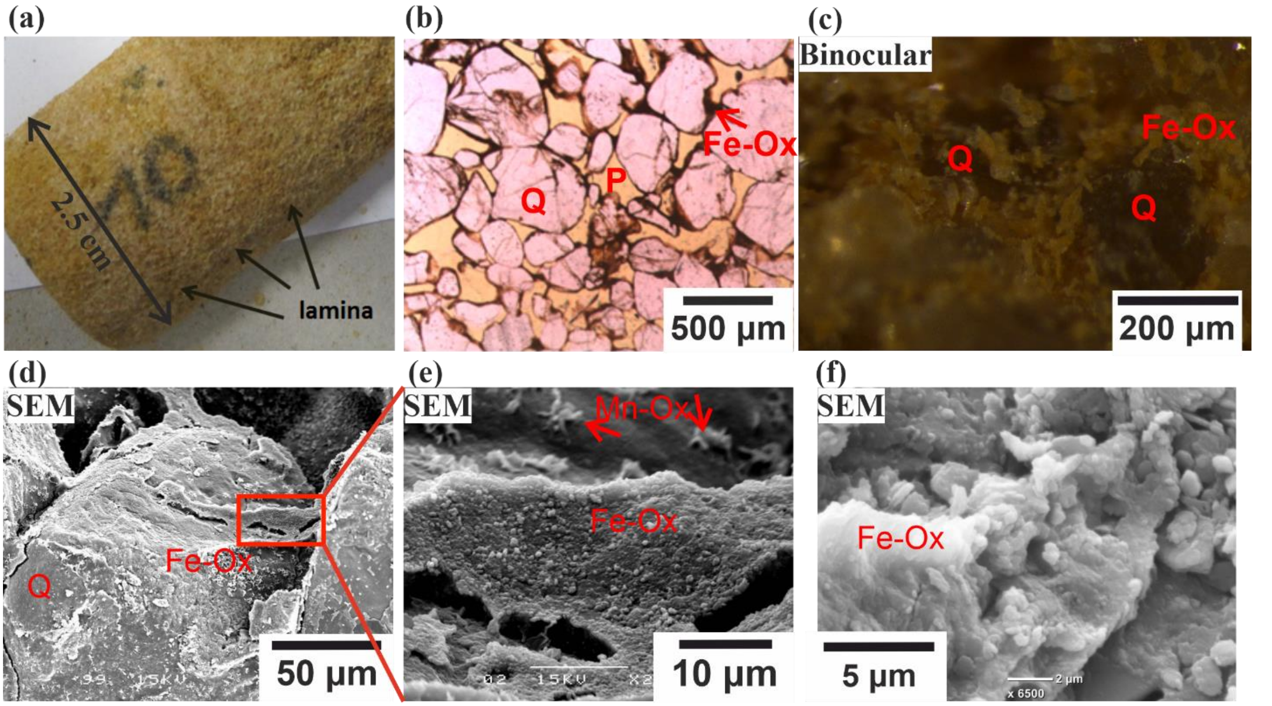

Figure 3: *Representative images of sandstone S1.* ***(a)*** *Darker laminae in the x-y plane at the millimetre scale are observed.* ***(b)*** *Thin section image of S1, P refers to open pores, Q – to quartz, Ox to oxide.* ***(c)*** *Fe-ox flakes (yellow) on quartz grains (pale grey).* ***(d)*** *SEM image of S1: grain-coating, meniscus-bridging cement and overgrowth of Fe-ox flakes.* ***(e,f)*** *Magnified images at different scales.*

Table 2. *Petrophysical characteristics of the three studied sandstone layers.*

	Method	S1	S2	S3
Grain size	Laser diffraction	325 µm **medium sand** **moderately sorted** sand: 92.6 % silt: 6.6 % clay: 0.8 %	154 µm **very fine sand** **poorly sorted** 65.7 % 31.3 % 3 %	269 µm **fine sand** **moderately sorted** 94.4 % 4.8 % 0.8 %
Pore throat size	MIP	Mode 1: 44 µm Mode 2: 0.035 µm Mode 3: 2.2 µm **macro pores** **well sorted**	0.035 µm 3.5 µm **meso pores** **poorly sorted**	35 µm 0.035 µm 2.2 µm **macro pores** **well sorted**
Pore size	Image analysis (min. object size 2.5 µm)	194 µm (*FWHM [150,335] µm)	Mode 1: 21 µm Mode 2: ~100 µm	223 µm (*FWHM [145,400] µm)
Characteristic length, l_c	MIP	42.9 µm	12.3 µm	36.9 µm
l_{max} contributing to maximal conductance	MIP	34.7 µm	8 µm	31.4 µm
Porosity, ϕ	Gas porosimetry	28 ± 2 % (7**)	19 ± 5 % (8)	31 ± 1 % (4)
	CT predicted image porosity from MIP	23.5 %	6.6 %	30.4 %
	Micro-CT segmented	17.5 %	6.9 %	28.3 %
Permeability, *κ* ⊥ - perpendicular to layering (z-direction) || - parallel to layering (x-y plane)	Gas permeametry	⊥ 350 mD (5) || 640 mD (2)	⊥ 2.77 mD (5) || 7.73 mD (3)	⊥ 220* mD (2) || 4600* mD (2)
	MIP	330 mD (1)	4 mD (1)	466 mD (3)
	Flow modelling	$\begin{pmatrix} 420 & 66.3 & 1.91 \\ 66.3 & 344 & 12.8 \\ 1.91 & 12.8 & 163 \end{pmatrix}$ mD	-	$\begin{pmatrix} 4517 & 5 & 38 \\ 5 & 4808 & 547 \\ 38 & 547 & 4085 \end{pmatrix}$ mD
Specific surface area, *SSA* (surface-to- bulk-volume)	MIP	3.2 μm^{-1}	12.2 μm^{-1}	0.16 μm^{-1}
Pore specific surface area, *PSA* (surface-to-pore-volume)	Micro-CT at 2.5 µm resolution size	0.068 μm^{-1}	0.136 μm^{-1}	0.069 μm^{-1}
Connectivity index	Image analysis	3.49	0.94	10
Tortuosity, τ	Flow modelling	-	-	x: 1.443 y: 1.393 z: 1.468
	Micro-CT shortest path analysis	x: 1.385 y: 1.373 z: 1.477	-	x: 1.316 y: 1.338 z: 1.394

Legend:

*Addressed in the Discussion.

** Numbers in parentheses related to gas porosity, gas permeability and MIP permeability, indicate the number of plugs for the measurements. Other measurements and calculations were conducted on single plugs.

FWHM - full width at half maximum, log-normal distribution.

Sandstone S2: The intermediate unit layer with a thickness of ~20 cm consists of grey-green moderately consolidated sandstone (Figs. 1c, 4) composed of sub-rounded to rounded, very fine sand grains (~154 μm); the sandstone is poorly sorted with 35 % of the particles being silt and clay (Figure 6, Table 2). Secondary silt (~ 40 μm), sand (~400 μm) and clay (~1.5 μm) populations are also detected. The grains are composed of quartz with minor Fe-ox coating the grains and minor quantities of heavy minerals (e.g., rutile and zirconium) (Figure 4c). Clay filling the pore space was identified by XRD as a kaolinite mineral. It appears as a grain-coating, meniscus-bridging, and pore-filling matrix (Figure 4b, c). Therefore, the unit layer (Figure 1c) is classified as a quartz wacke sandstone (Pettijohn et al., 1987).

The pore space is reduced by clays deposited on coarser grains, identified mostly in laminae (Figure 4a, d). However, the inter-granular connectivity of macro pores can still be recognized (Figure 4b, c). The effective pore network consists of inter-granular macro pores distributed between the laminae or zones richer in clay and Fe-ox. Integrating the grain size and pore throat size analysis results (Figs. 6, 7) confirms that the reduction in the inter-granular pore space in S2 is due to the clay matrix, which is reflected in the poor grain sorting and large variance in pore size. In the pore throat size analysis (Figure 7), only 15 % of the pore volume is composed of macro pores that are larger than 10 μm. The prominent sub-micron pore mode is ~35 nm, with a population containing ~45 % of the pore volume (Figure 7a). This population of pores occurs inside the clay matrix. The secondary pore volume population is poorly distributed within the range of 0.8-30 μm. The characteristic length (Sect. 3.2), $l_c = 12.3$ μm (Figure 7b), and the pore throat length of maximal conductance, $l_{max} = 8$ μm (Appendix B, Figure B1) (both have a large uncertainty resulting from uncertainty in the threshold pressure), suggest a connectivity of macro pores regardless of their small fraction within the total pore space. The porosity of S2 evaluated for 8 different samples varies in the range of 14.5-23.5 % (Figure 8). From the *PTSD* (Table 1) and gas porosimetry results (for a sample with a porosity of 18.6 %), micro-CT predicts an image porosity of 6.6 % at a resolution limit of 2.5 μm (Table 2). The gas permeability in the z-direction was measured in 5 samples (Figure 8): in four of them, the permeability ranges within 1-12 mD and increases with porosity. However, one sample had an exceptionally large porosity and permeability of 23 % and 62 mD, respectively. The permeability measured for 3 samples in the x-y plane ranges within 4-12 mD, also showing ~15 % porosity (Figure 8). In addition, for the samples with ~15 % porosity, their permeability is ten times larger in the x-y plane (parallel to the layering) than in the z-direction (perpendicular to the layering). The permeability derived from MIP reaches 4 mD, which agrees with an average of 2.77 mD and 7.73 mD (Table 2) measured in the z-direction with a gas permeameter (excluding one exceptionally high value, Figure 8).

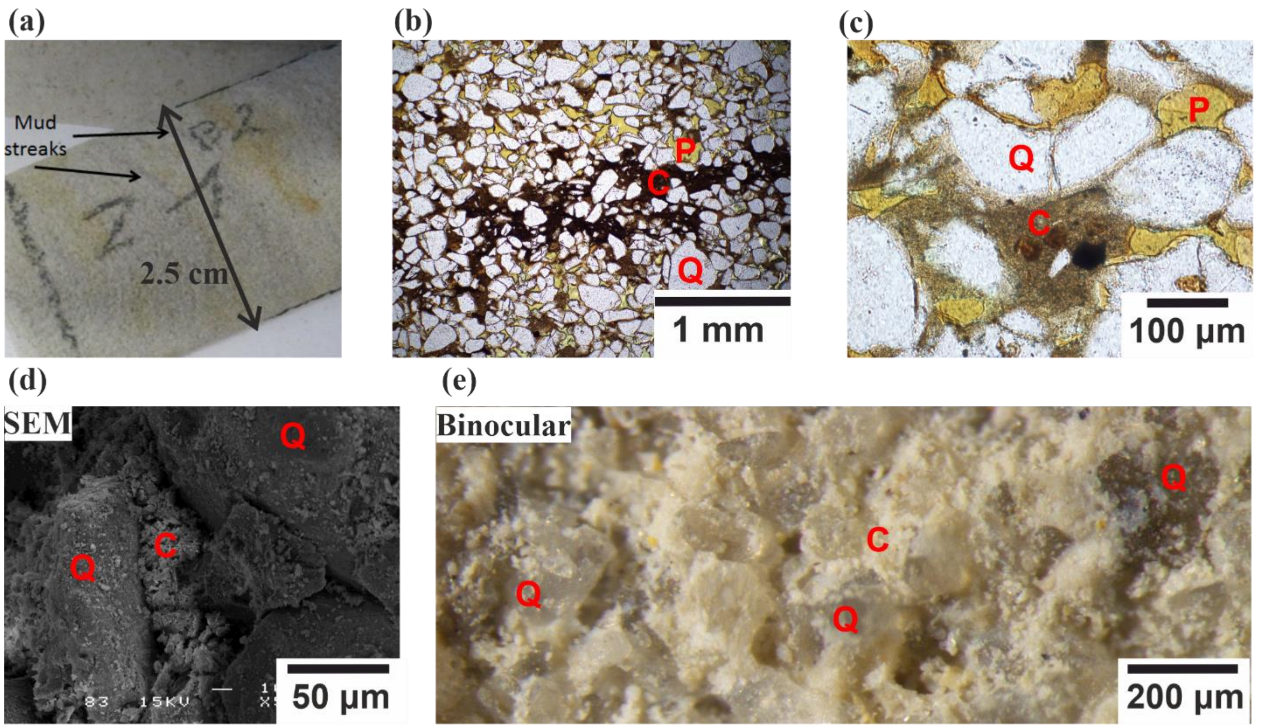

Figure 4. Representative images of sandstone S2. ***(a)*** *Dark stains in the rock are mud streaks, yellowish zones are due to increased Fe-Ox cement.* ***(b)*** *The dark laminae are richer in clays and Fe-ox. P refers to open pores, Q – to quartz, C – to clay.* ***(c)*** *Clay and silt accumulated as meniscus and as clay matrix.* ***(d)*** *Pore clogged by clay and Fe-ox.* ***(e)*** *Rock texture. The clay matrix is white, and quartz grains are pale grey.*

<u>Sandstone S3</u>: The bottom unit layer with a thickness of ~1.5 m consists of (pale) red-purple poorly consolidated sandstone (Figure 1c) with grains covered by a secondary red patina (Figure 5). The sandstone is composed of friable to semi-consolidated, fine (~269 µm), moderately sorted sand (Table 2), where only

5.6 % of particles are silt and clay (Figure 6). Secondary silt (~ 50 μm) and clay (~ 0.96 μm) populations were also detected. The sandstone consists of sub-rounded to rounded grains showing a laminated sedimentary texture consisting of the cyclic alternation of relatively dark and light red bands of millimetre-scale thickness (Figure 5a). The dark laminae contain slightly more Fe-ox meniscus-bridging and pore-filling cementation (Figure 5b, d). Overall, this bed consists of a ferruginous quartz arenite. The grains are dominated by quartz with very minor feldspar and black opaque mineral grains, perhaps Fe-ox (Figure 5d). X-ray diffraction indicated quartz only. The Fe-ox coating of grains is less extensive than in other samples (Figure 5c). The pore interconnectivity in this sandstone is high (Figure 5d). Heavier cementation is rarely observed (Figure 5d) and is organized in horizontal laminae (Figure 5a). Features including grain cracks, grain-to-grain interpenetration, and pressure solution are also recognized (Figure 5e). The *PTSD* showed that 95 % of the pore volume is presented by macro pores (Figure 7a), which agrees with the minority of fine particles. The characteristic length and pore throat length of maximal conductance are $l_c = 36.9$ μm (Figure 7b) and $l_{max} = 31.4$ μm (Appendix B, Figure B1), respectively.

The porosity measured by a gas porosimeter in the laboratory varies in the range of 30-32 % for 4 different samples (Figure 8). From *PTSD* and gas porosimetry (Figs. 7, 8), the micro-CT-predicted image porosity at a resolution limit of 2.5 μm is 30.4 % (Table 2). The permeability measured by a laboratory gas permeameter averages 220 mD for 2 samples measured in the z-direction and 4600 mD for 2 samples measured in the x-y plane (Figure 8), showing a ten-fold difference (discussed in Sect. 5). The permeability derived from MIP reaches 466 mD (Table 2).

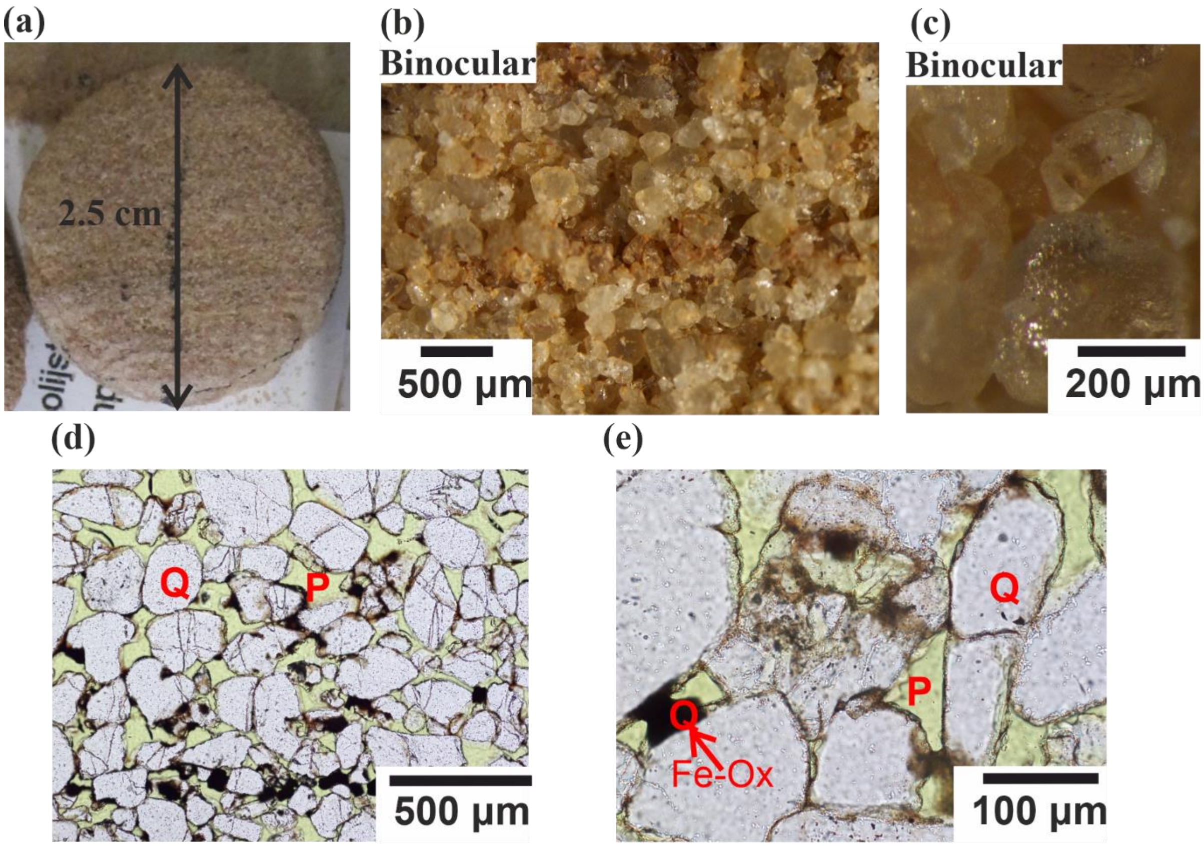

Figure 5. Representative images of sandstone S3. (a) Laminae are recognized by their slightly dark and red color. (b) General view reveals red laminae ~300 µm thick. (c) High-resolution observation of a clear grain. (d) A millimetre-scale lamina is indicated by enhanced meniscus-type Fe-ox cementation and partly by inter-granular fill. Grain surfaces are coated by thin Fe-ox. Black and orange cements represent crystallized and non-crystallized Fe-ox, respectively. Some cracked grains are observed, sporadically cemented by Fe-ox. P refers to open pores, Q – to quartz. (e) Partially dissolved grains are coated by cement.

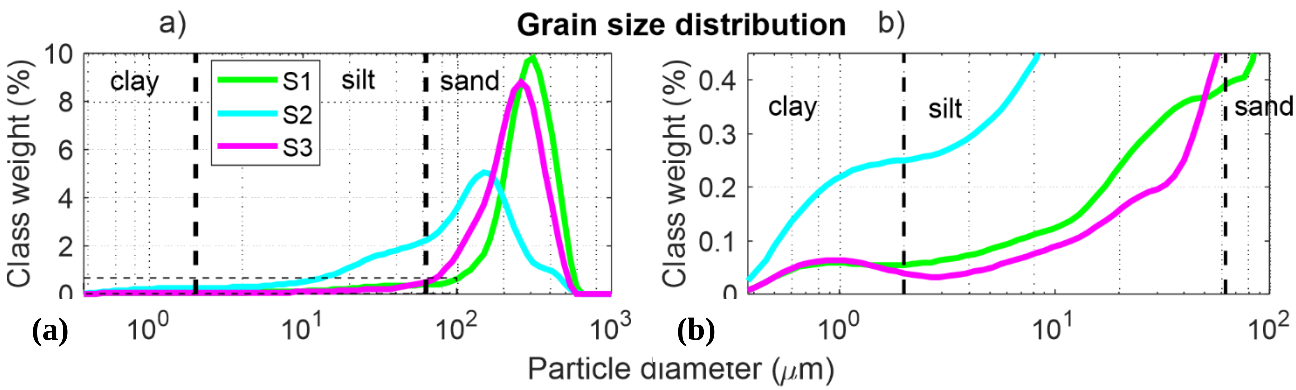

Figure 6: ***(a)*** *Grain size distribution.* ***(b)*** *Magnified grain size distribution in the fine grain size region plotted for sandstones S1 (green), S2 (blue) and S3 (purple). S1 and S3 have a unimodal distribution and are moderately sorted with a small skewness tail. Sample S2 has a multi-modal distribution and is poorly sorted.*

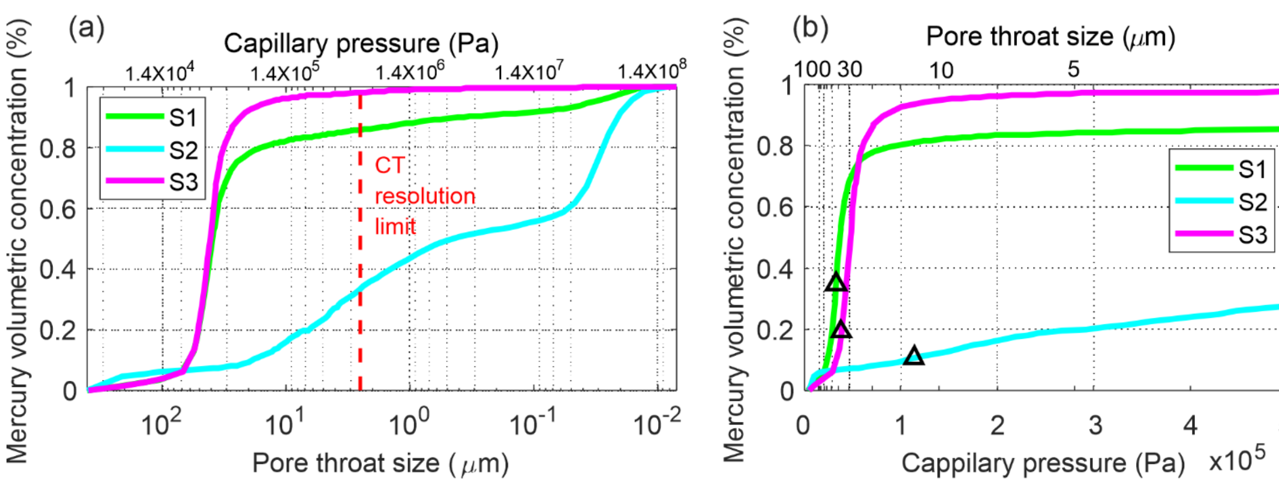

Figure 7: *Cumulative pore throat sizes of the studied sandstones.* ***(a)*** *Capillary pressure on a logarithmic scale. The resolution limit of the micro-CT imaging indicates the fraction of the pore space that could be resolved.* ***(b)*** *Capillary pressure on a linear scale. The triangles indicate the characteristic length,* l_c.

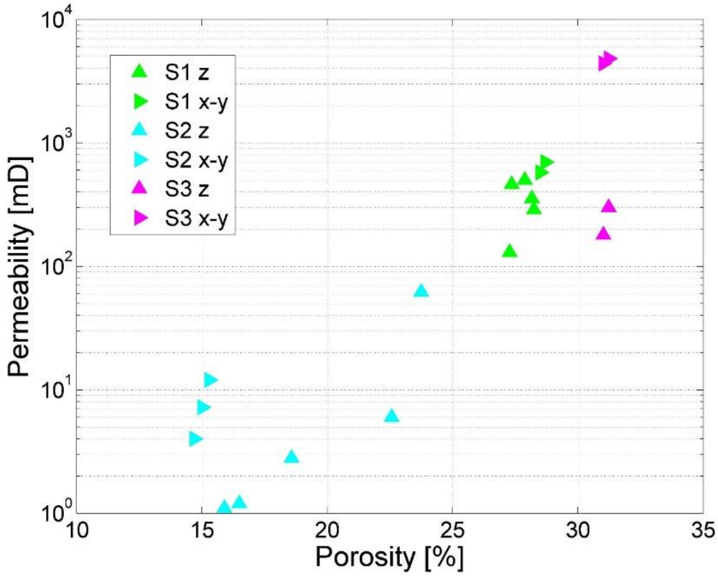

Figure 8: *Results of porosity-permeability lab measurements. The permeability of the samples was measured in directions perpendicular to the bedding (z-direction) and parallel to the bedding (x-y plane).*

Overall, for all three investigated sandstones, the pore throat size contributing to the maximal conductance, l_{max}, is smaller than the characteristic length, l_c (Table 2), when the relative decrease is greater for the layers containing more fines.

Additionally, pore surface roughness may be evaluated from the specific surface area (*SSA*) measured by MIP (Table 2). A larger *SSA* implies a rougher surface (e.g., Tatomir et al., 2016). The *SSA*s for S1 and S2 (3.2 μm^{-1} and 12.2 μm^{-1}, respectively) are similar to those given in the literature for sandstones of similar properties (e.g., Cerepi et al., 2002). The *SSA* of S2 is higher because of its high silt and clay content of 34.3 %, which is only 7.4 % for S1 (Figure 6a). The *SSA* of S3 (where silt and clay constitute only 5.6 %, including the Fe-ox rim coating) is only 0.16 μm^{-1}, which is 20 times smaller than that of S1 (Table 2). The difference in *SSA*s between S1 and S3, which are similar in their grain and pore throat size distributions (Figs. 6, 7), is a result of S1 having a higher Fe-Ox grain coating than S3 (compare Figs. 3d and 5c).

In summary, although the S1 pore network has larger pore throats, it also has greater grain roughness and lower connectivity than S3. These two properties dominate and generate a smaller permeability for S1 than for S3 (Table 2).

4.2. Image analysis

Visualized segmented sub-volumes of samples S1, S2, and S3, depicting Quartz, pores, clay and heavy minerals, are presented in Figure 9. The main pore size population in PSD of S1 is at ~100-500 μm range with majority at 194 μm (Figure 10). A smaller population of pores of ~30-100 μm was identified as well, which may refer to (Mode 1) pore throat size derived from the MIP experiment (Table 2). Image resolution of 2.5 μm limited the analysis. The pore specific surface area (*PSA*) calculated from micro-CT images is $0.068\ \mu m^{-1}$. The tortuosity, measured from the whole CT image, indicates similar values in the x- and y-directions of 1.37 and 1.38, respectively, whereas in the z-direction, the tortuosity is 1.48 (Table 2). As many paths were considered, this difference indicates the textural features that appear in horizontal plane (Figure 3a).

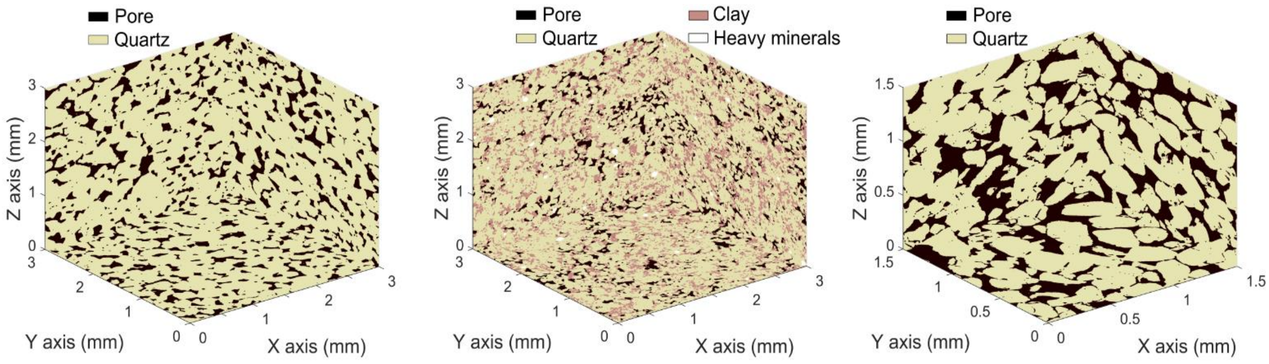

Figure 9: *Visualized sub-volumes of segmented CT samples of (a) S1, (b) S2, (c) S3. S1 and S2 in this visualization have volumes 3^3 mm^3 scanned with 5 µm voxel size resolution, S3 has volume 1.5^3 mm^3 scanned with 2.5 µm voxel size.*

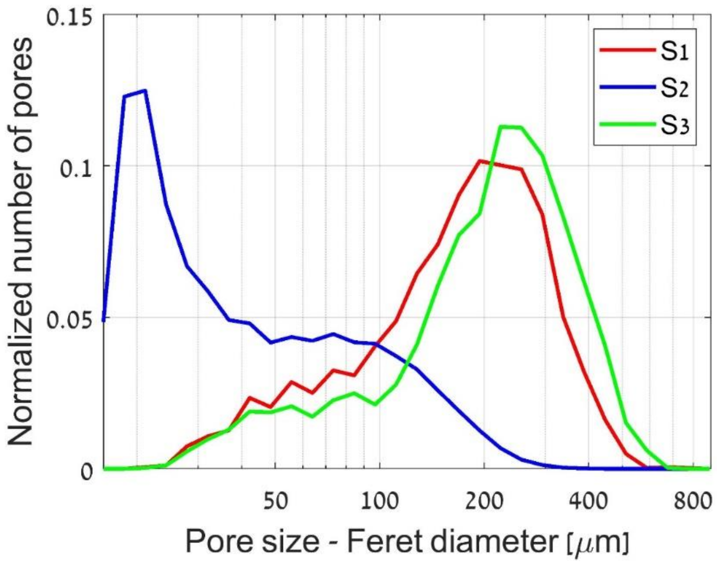

Figure 10: *Statistics of the pore sizes calculated by image analysis for three sandstone samples: S1, S2, and S3. Number of pores analysed: S1 – 3500, S2 – 45000, S3 – 3500. The CT samples used for this analysis had 2.5 µm voxel size resolution.*

For S2 (Figure 9), the main pore size population is at ~15-50 µm range (Figure 10), with majority at 21 µm. This may refer to the pore throat size derived from MIP. However, smaller pore throat sizes which were derived from the MIP (mode peak is at ~3.5 µm) could not be visualized due to the limited resolution of the image (2.5 µm), and because of high uncertainty associated with size of pores smaller than 10 µm (four voxels) (that were excluded from the PSD evaluation, Figure 10). A large pore population is also recognized at ~100 µm (Figure 10), which corresponds to the pore size scale recognized from the petrography (Figure 4), MIP (Figure 7) and CT image (Figure 9). The pore specific surface area (*PSA*) calculated from micro-CT images is

$0.136\ \mu m^{-1}$ (Table 2), which is twice as large as the *PSA* of S1.

For S3 (Figure 9), the main pore size population is at ~100-500 μm range (Figure 10), with majority at 223 μm. The geometry-based tortuosity values measured from the whole CT image with multiple paths is 1.32, 1.34 and 1.39 in the x-, y- and z-directions, respectively. The tortuosity is lower for S3 than for S1 in all directions, which is a direct result of the smaller amount of cement in the pore throats. The *PSA* of S3 is $0.069\ \mu m^{-1}$, which is similar to that of S1.

4.3 REV Analysis

4.3.1. Quartz arenite sandstones (S1 and S3)

One-dimensional profiles of porosity (Figure 11(a-c)) were evaluated in sequential slices in three orthogonal directions of S1, having a maximal available segmented volume of $6.8 \times 6.9 \times 9.2\ mm^3$ scanned with a voxel size of 5 μm (suitable for imaging pore throats that effectively contribute to the flow in S1, Table 2). The slice-by-slice porosity distinguishes the z-direction as having an exceptional behaviour, with variance in porosity fluctuations being four times larger than that in x- and y- directions. Porosity fluctuates around the mean value with a wavelengths of ~0.2 mm in x- and y- directions. Semivariograms (obtained after z-score transformation of porosity histograms, Figure 11d) show stationarity in x- and y- directions (i.e., sill~1, Figure 12). The nugget is set to zero (see Methods Sect. 3.2). A semivariogram was fitted using Gaussian model with range of ~0.1 mm for x- and y- directions (Figure 12a,b). A second semivariogram feature is the waviness, i.e. cyclic behaviour with lag distance. The lag distances of the first peaks in the experimental variograms are 0.135 and 0.15 mm in x- and y- directions, respectively. In laminated geologic settings, the distance to the first peak is an indication of the average thickness of the bedding in that direction (Pyrcz and Deutsch, 2003). However, here this distance refers to the average size of the cross sections of pores in this direction (a cross-section varies from zero to the maximal one), which is smaller than the average pore size measured in image analysis. The lag distance between the peaks is about 0.2 mm, being similar to that observed in Figure 11a,b that refers to the average cross-section of pores and grains in that direction. In z-direction (Figure 11c, black line) the variability is larger than in x- and y- directions, depicted by a cyclic structure with ~3.5 mm wavelength. A cyclic structure with lower amplitude and smaller wavelengths in z-direction “rides” on the main structure with a higher wavelength. A trend in porosity increase with distance is observed, being modelled by a linear regression model (0.166 % porosity per mm), which was removed from the original porosity (in black) to obtain the porosity residuals (in red, Figure 11c). The experimental semivariogram of the residuals (Figure 12c, in red) shows smaller sill and range than the semivariogram of the original porosity (in black). The semivariogram in z-direction was fitted with two nested models, a Gaussian model with range of 0.1 mm similar to those applied to x- and y- directions, and a hole-effect model with range of 1.63 mm. The hole-effect range refers to the average thickness of horizontal layering structures of mm-scale, comprising larger or smaller grains, which impose larger or smaller pores between them (see sample cross-section in microscopy in Figure 3b). The first trough at 3.4 mm lag distance (Figure 112c) in the curve with a larger wavelength, refers to the average thickness of these two layers with higher and lower porosity. A secondary structure in the semivariogram of the lower wavelength of ~0.2 mm is similar to those observed in x- and y- directions. The larger-scale layering is discerned in z-direction only, and the larger variance of porosity in that direction implies an anisotropy in a sandstone S1.

In order to capture this layering pattern, a volume with a side length of at least ~3.5 mm in z-direction is required. The ranges in x- and y- directions of ~0.1 mm are associated with the typical pore sizes, which are too small to be used in flow modelling, as to predict the permeability reliably, it is necessary to capture the three-dimensional tortuosity of the pore space. Alternatively, the REV size from the classic approach, was estimated as ~1.2 mm (Appendix A, Figures A1a, b). Therefore, for the flow simulations, we decided to use a segmented specimen cube with a maximal available edge length of 2950 μm, scanned with a higher resolution of a 2.5 μm, to preserve a consistency between the flow simulations in S1 and S3.

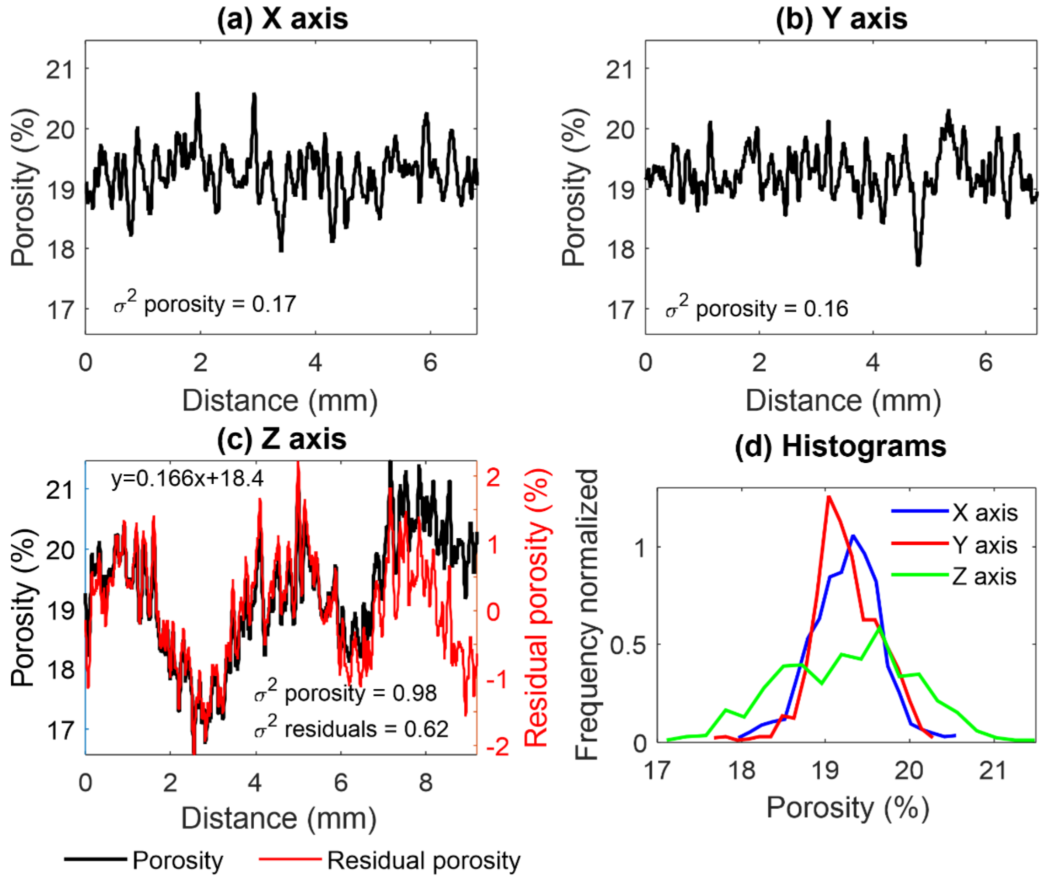

Figure 11: *One-dimensional porosity profile of S1 slices evaluated in a) x-direction, b) y-direction and c) z-direction. Investigated volume size is 6.8 × 6.9 × 9.2 mm^3. For z-direction, the right y-axis refers to the residual porosity after removing the trend, modelled by a linear regression model. The porosity variations both before (in black) and after (in red) the trend removal are demonstrated. (d) Porosity histograms (z-direction after the trend removal).*

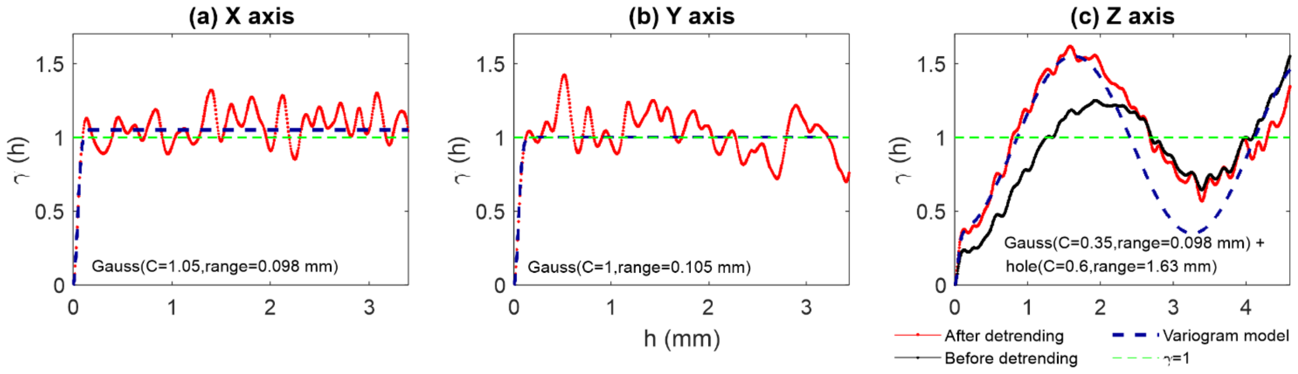

Figure 12: *Semivariograms of S1 in a) x-direction, b) y-direction and c) z-direction. z-score transform was applied to the histograms (Figure 11d). For z-direction it was applied before (in black) and after (in red) the trend removal (Figure 11c). The variogram analytical models (Gaussian and hole-effect) are also displayed (dashed blue line), modelled with nugget set to zero.*

One-dimensional profiles of porosity were evaluated in sequential slices in the orthogonal directions of S3 with a maximal segmented volume of $3 \times 3 \times 4.2\ mm^3$ scanned with a voxel size of 2.5 μm (Figure 13a-c). Porosity fluctuates around the mean with no trend in all directions. Modelling of the experimental semivariograms (Figure 14) shows stationarity in the investigated domain with range of ~0.087 mm, smaller than that in sample S1 (~0.1 mm). Cyclic structure contributes to ~40 % in the semivariogram variability. The first peak in x- and y-directions are at ~0.115 mm and in z-direction it is at ~0.103 mm, which relates to the average size of pore cross-section in that direction. The first trough at ~0.2 mm in all directions, relates to the average cross section of pore and grain together in those directions. Porosity variance in z-direction is ~1.08 that is slightly larger than that in other directions (~ 0.9). However a distinct difference in the spatial variability as that in S1 is not observed, which implies that S3 has lower anisotropy characteristics.

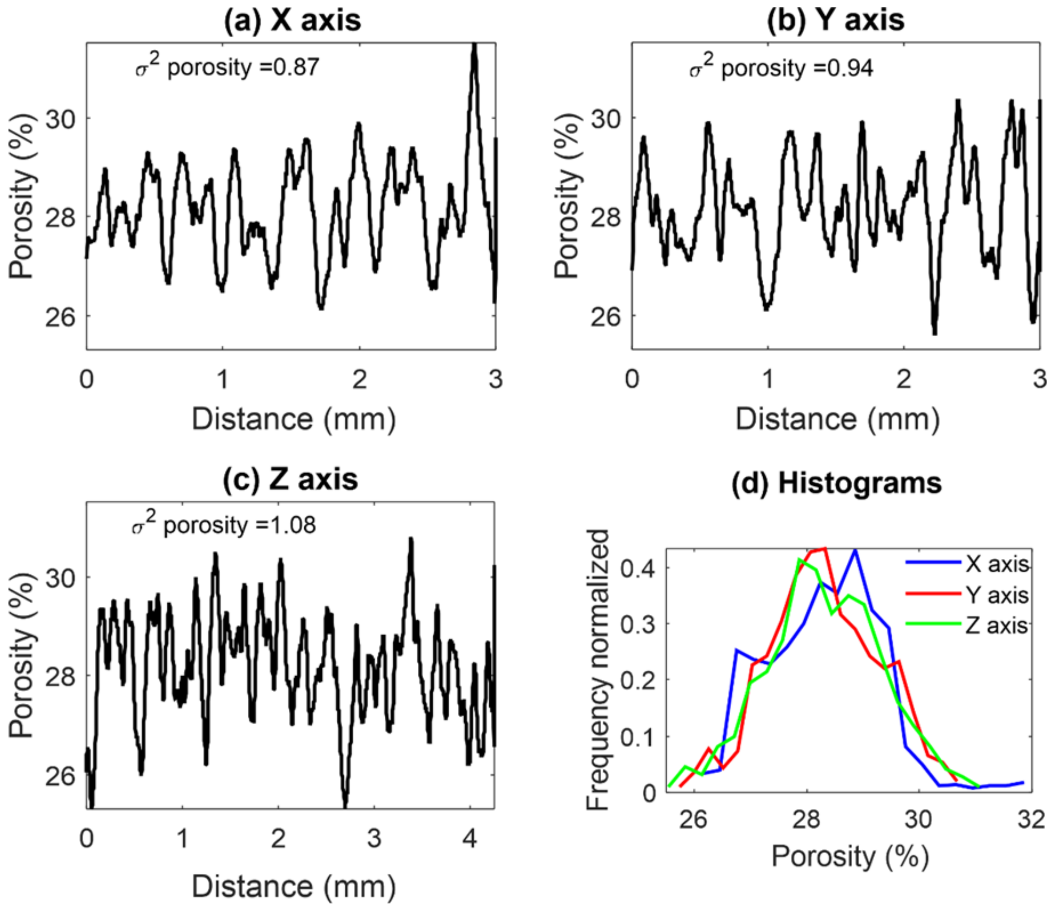

Figure 13: *One-dimensional porosity profile of S3 slices evaluated in a) x-direction, b) y-direction and c) z-direction. Investigated maximal segmented volume size is 3 ×3 ×4.2 mm^3 . d) Porosity histograms.*

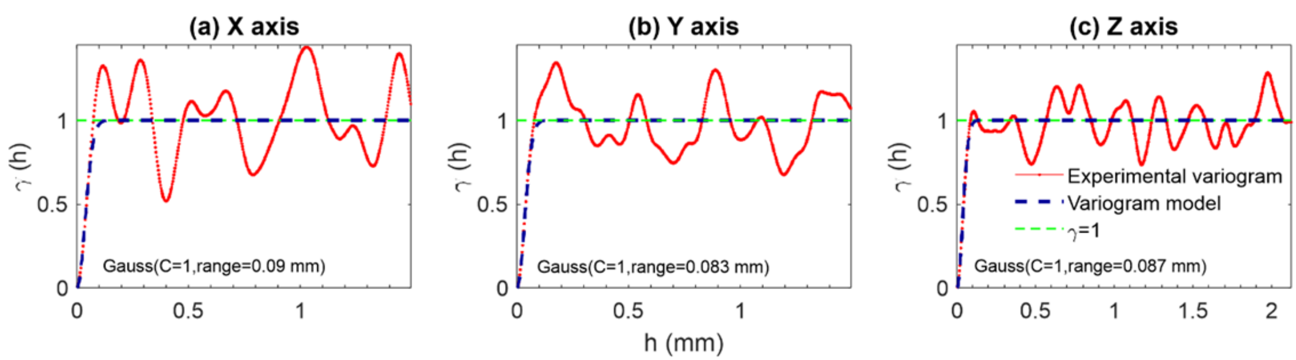

Figure 14: *Semivariograms of S3 in a) x-direction, b) y-direction and c) z-direction. The experimental semivariogram was modelled using Gaussian model (dashed blue line). The semivariogram models are also displayed, modelled with nugget set to zero.*

Classic REV porosity analysis (Appendix A, Figure A1e,f) yields REV size with a cube edge length of 875 μm (350 pixels), which is about ten-fold larger than the ranges observed in the semivariogram analysis (~0.1 mm, which is a typical size of a pore). For the same reasons used in estimations of REV by the classic approach in S1, the classic REV derived volume was used for the flow modelling in S3.

4.3.2. Quartz wacke sandstone (S2)

Sample S2 is more heterogeneous than S1 and S3 because of the deposition of clay. The sample is visualized in Figure 9b with quartz grains (yellow), pore volume (black), clay matrix (brown) and heavy minerals (white). The clay matrix is distributed in patches. In Figure 15, the porosity of sequential planes in the orthogonal directions is shown together with clay matrix content. In z-direction a clear trend in porosity is observed, which has a negative correlation with the clay content (Figure 16), whereas in the horizontal (x-y) plane there is no clear correlation. This correlation in z- direction implies that the porosity is controlled by the depositional processes (However, the similar large-scale wavy structures of the clay content in x- and y-directions (Figures 15a,b) may refer to errors originated from the scanning and inversion in the CT acquisition, as x- and y-coordinates are associated with the side boundaries of the cylindrical sample). The trend was removed in all three directions to remain with residual porosity, when the largest trend slope was in z-direction (Figure 17). After the trend removal, the histogram variance in x- direction appears as the largest one, more than twice larger than that in y-direction. Semivariogram analyses were performed (Figure 18) to investigate the spatial variability of the entire available 3D volume (7.9 × 6.8 × 9.2 m^3) scanned with 5 µm resolution. Experimental semivariograms were calculated twice: on porosity values, and on porosity residuals (both the porosity and residuals are z- score transformed before calculating the semivariogram). After the trend removal, the range and sill decrease in all directions and especially in z-direction that now reaches the sill. In x-direction the detrended semivariogram keeps increasing above sill of 1 for the increasing lag distance, thus indicating that the trend was not completely removed, and that the domain is not fully stationary. The semivariograms have multiple structures including cyclicity, therefore, three analytical nested models were used in all directions: Gaussian, spherical and hole-effect models. The smallest range for the y- and z- directions (Figure 18) is within 0.062-0.07 mm, which refers to the average size of pore cross-section, in agreement with the pore size distribution from the image analysis (Figure 10), which is smaller than those of the S1 and S3. However, the contribution of the pore size scale to the overall variability (0.2-0.35) is smaller than that in S1 and S3. The ranges of the larger-scale cyclic structure are ~1.1 mm and ~2.1 mm in horizontal and vertical directions, respectively. These length scales relate to an average thickness of the more porous "lenses" originated at the presence of patchy clay deposition. An intermediate range between those from the Gaussian and hole-effect models in y- and z- directions are of ~0.35 mm discerned by a spherical model, may relate to another structure, associated with a distance between pores.

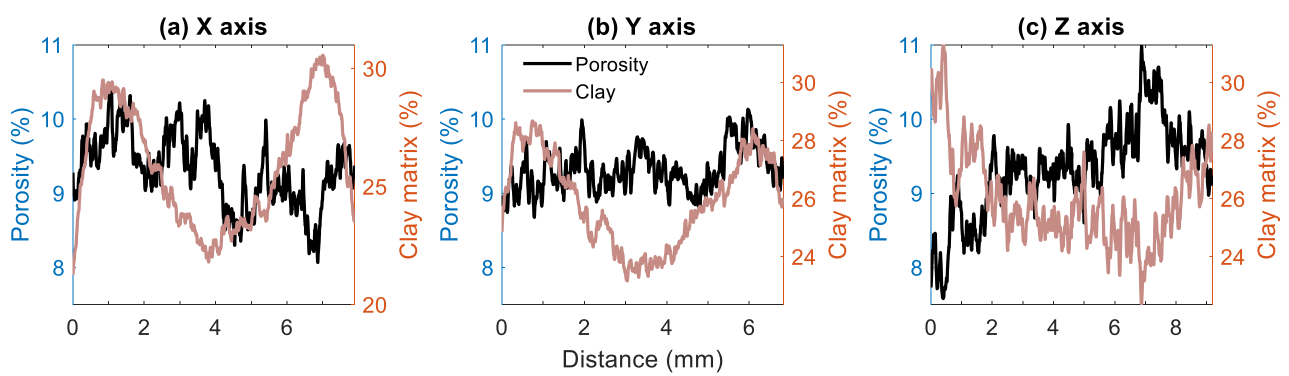

Figure 15: *Porosity (left) and clay (right) profiles in slices of S2 evaluated in (a) x-direction, (b) y-direction (c) z-direction. Investigated maximal segmented volume size is* 7.9 × 6.8 × 9.2 m^3 *(see text for more detail).*

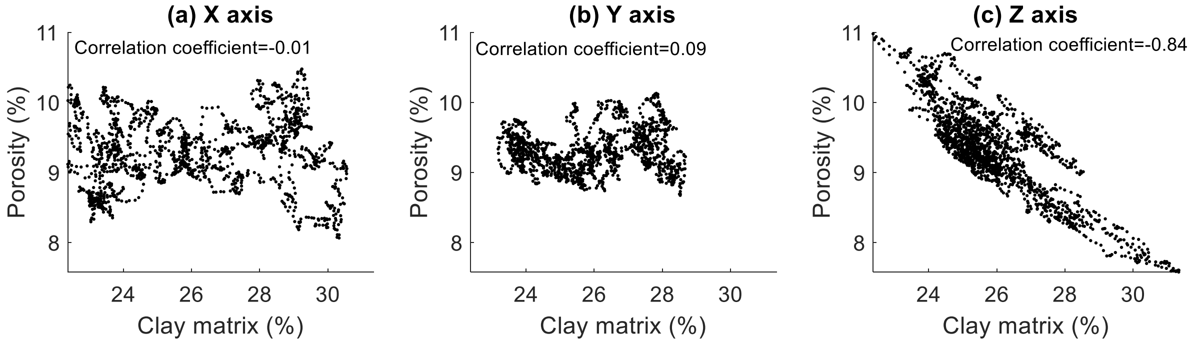

Figure 16: *Scatterplots of clay content and porosity in S2 in (a) x-direction, (b) y-direction, (c) z-directrion.*

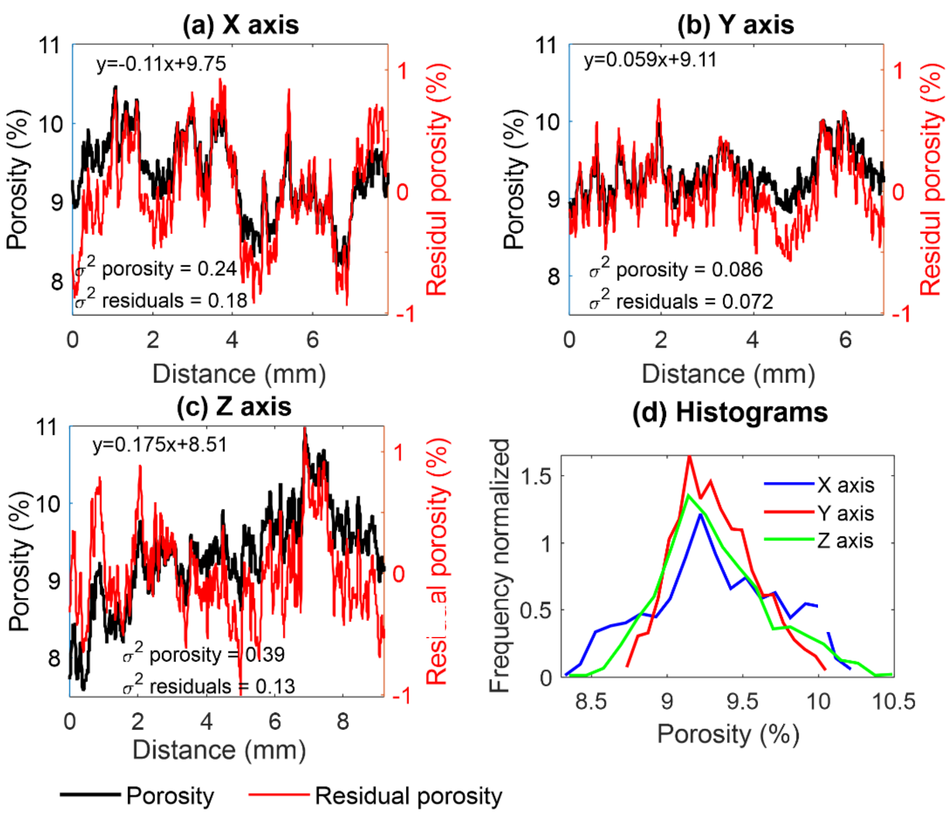

Figure 17: *One-dimensional porosity profile of S2 slices estimated in a) x-direction, b) y-direction and c) z-direction. The left vertical axes of the panels refer to the real porosity values, while the right axes to the*

residual porosity after removing the trend, modelled by a linear model, shown in each subplot. The variances before and after the trend removal are indicated. (d) Porosity histograms after the trend removal.

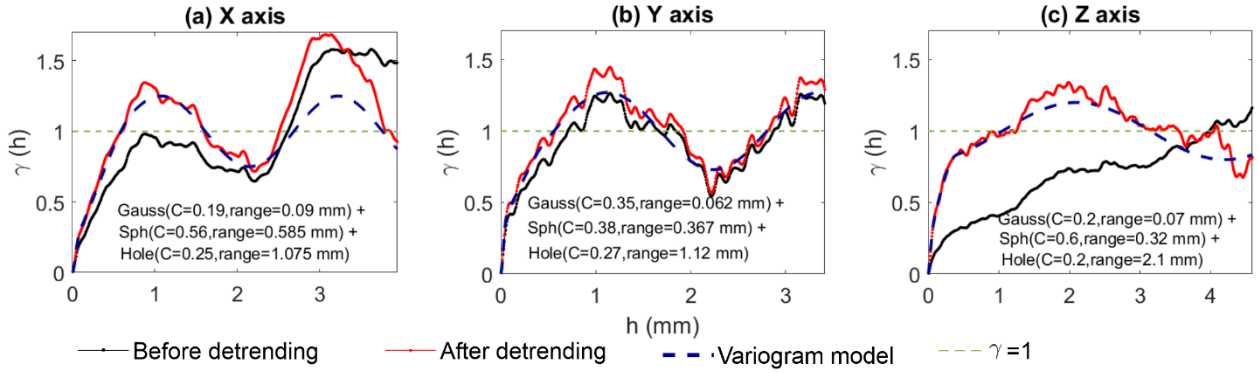

Figure 18: *Semivariograms of S2 in a) x-direction, b) y-direction and c) a-direction. z-score transformation was applied to the histogram, before (black) and after (red) the trend removal. The experimental semivariogram was also modelled using nested Gaussian, spherical and hole-effect models (dashed blue line) with nugget set to zero. The calibrated sill and range are shown (see text for more detail).*

Alternatively, the large difference between the mean and median porosities is identified by the classic porosity-based REV approach (Appendix A, Figure A1c, d). Together with the porosity trend in z-direction (Figure 15) in the volume under investigation (7.9 × 6.8 × 9.2 m^3), there is no REV in S2. As a result, flow modelling could not be conducted in sample S2.

Additionally, there is an opportunity to investigate a heterogeneity of S2 by analysing semivariograms for the sequential slice porosity for the multiple sub-volumes of the volume investigated above (7.9 × 6.8 × 9.2 m^3 size, Figure 19). For each sub-volume cube (with 3.5, 1.2, and 0.5 mm edge size) the trend in porosity was removed and the histogram was standardized. A threshold was set such that only the stationary semivariograms were analysed to calibrate the range of correlation. This threshold is associated with sills between 0.9 and 1.1.

For 3.5^3 mm^3 sub-volumes (Figure 19a-c), with an edge size 2-3 times larger than the cyclic range found (1.1 mm in x- and y- directions, 2.1 mm in z- direction, Figure 18), and which is about half the size of the entire domain (7.9 × 6.8 × 9.2 mm^3), the spherical model was used, and the percentages of passing the threshold were 39, 33 and 12 % in x-, y- and z-directions, respectively. The average residual variances were

0.39, 0.34 and 0.59, respectively. Experimental semivariograms were chosen randomly for the observation (Figure 19a-c). The semivariograms vary in all directions (indicated by the variability in slopes till reaching the ranges), when the calibrated ranges averaged to 204±65 µm, 202 ±69 µm and 334 ± 137 µm, for x-, y- and z- directions, respectively. The large cycles of more than 1 mm in the wavelengths are not consistent. Overall, for 3.5^3 mm^3 sub-volume sizes, the ranges in x- and y-directions do not vary much, but z-direction shows a smaller percentage of sub-volumes passing a sill threshold and a larger variance, which points on more heterogeneous and irregular structure of the pore space.

Modelled 1.2^3 mm^3 sub-volumes (Figure 19d-f) are smaller than the cyclic length calibrated for the entire domain (Figure 18). Gaussian model, which fits the smallest range structures in the entire domain, was used. The percentage of the sub-volumes which passed the threshold were 35, 42 and 17 % in x-, y- and z-directions, respectively. The average residual variances were 1.76, 1,59 and 3.27, respectively. The semivariograms initial slopes (Figures 19d-f) vary mainly in z-direction, when the calibrated ranges averaged to 79±18 µm, 72 ±19 µm and 187 ± 120 µm in x-, y- and z- directions, respectivelly.

For the smallest 0.5^3 mm^3 sub-volumes (Figure 19g-i), the percentages which passed the threshold were 27, 30 and 11 % in x-, y- and z-directions, respectively. The average residual variances were 4.6, 4.8 and 12.3. The semivariogram initial slopes (Figure 19g-i)vary more in z-direction, when the calibrated ranges averaged to 43±8.3 µm, 43 ±9 µm and 91 ± 44 µm in x-, y- and z- directions, respectively.

To summarize, small percentages of sub-volumes which passed the stationarity threshold imply that the sub-volumes of those sizes are not representative for S2. For the increasing sub-volume sizes the range increases (Figure 19), because larger sub-volume is composed of smaller sub-volumes with very different structure characteristics, including those that have not passed the threshold. The larger range identified in z-direction is assumed to be related to an irregular structure in that direction, whereas in x- and y- directions the heterogeneity is milder. The larger porosity variance in z-direction implies an anisotropy due to less constrictions to flow in the horizontal plane.

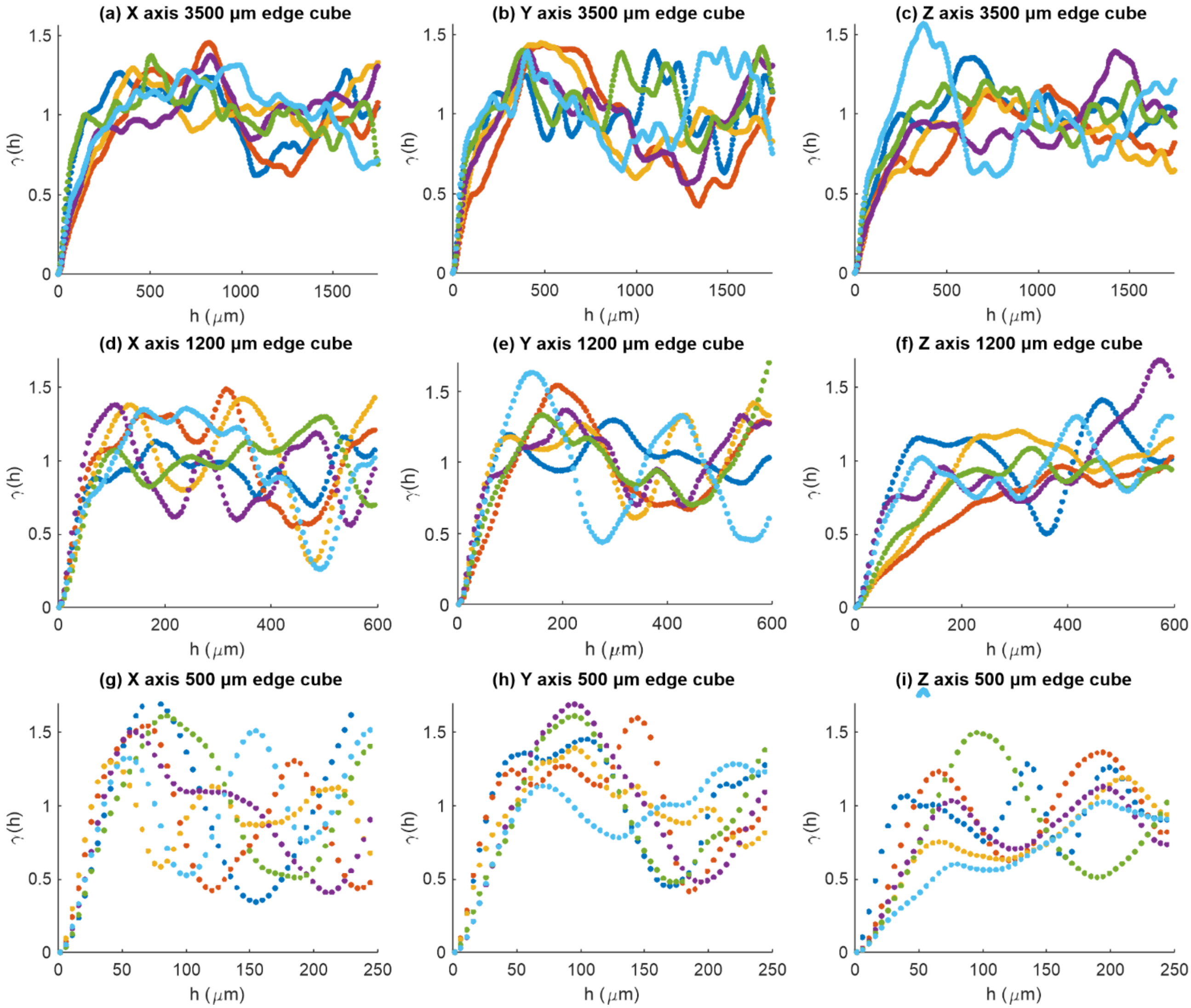

Figure 19: *Experimental semivariograms of sub-volume cubes with* 3.5^3 *mm*^{3} *(top row),* 1.2^3 *mm*^{3} *(middle tow) and* 0.5^3 *mm*^{3} *(bottom row) edge sizes, in x-direction (left column), y-direction (middle column) and z-direction (right column), respectively.*

4.4. Flow modelling at the pore scale

Fluid flow was modelled at the pore scale in two different micro-CT-scanned geometries: 1) a full cube of sample S1, and 2) sample S3 within its REV dimensions (Table 3), imaged with 2.5 µm voxel size.

Modelling of the 3D geometry of sample S2 was not performed due to its non-stationarity which did not allow finding the REV in the investigated domain.

Table 3. *Porosity losses in S1 and S3 over the course of applying the extended computational workflow (*Figure *2).*

Sample	Sample size (mean mesh edge size) [μm]	CT segmented image porosity (%)	Connected porosity (%)	Mesh porosity (%)	Gas porosity (%)
S1 (entire sample, 1180 voxels)	2950 (14)	17.5	15.6	13.6	28
S3 (REV, 350 voxels)	875 (5)	28.3	27.9	25.9	31

The porosity of the meshed domain of sample S1 is 13.6 % (in contrast to 17.5 % in the segmented image, Table 3), and the mesh edge length is 14 µm along the pore walls. The observed porosity loss results from disconnecting narrow pore throats from the connected cluster imaged with a 2.5 µm voxel size due to the use of a 14 µm mesh size (the lowest possible for our computational needs). A maximum Reynolds number of $Re = 0.084$ was used to guarantee the simulation in a creeping flow regime.

The symmetrized permeability tensor, $\bar{\bar{\kappa}}$, was obtained as follows (Table 2):

$$\bar{\bar{\boldsymbol{\kappa}}}_{\boldsymbol{sym}} = \begin{pmatrix} 420 & 66.3 & 1.91 \\ 66.3 & 344 & 12.8 \\ 1.91 & 12.8 & 163 \end{pmatrix}$$

The permeability tensor is anisotropic, with κ_{zz} being more than half κ_{xx} and κ_{yy}. This result is in agreement with the appearance of horizontal banding with higher cementation derived from the semivariogram analysis (Figure 11c).

The porosity of the meshed domain of sample S3 is 25.9 % (in contrast to 28.3 % in the segmented image, Table 3), and the mesh edge length is 5 µm along the pore walls. A maximum Reynolds number of $Re = 0.22$ was used to guarantee the simulation in a creeping flow regime. The symmetrized permeability tensor is close to isotropic (Table 2):

$$\bar{\bar{\boldsymbol{\kappa}}}_{sym} = \begin{pmatrix} 4517 & 5 & 38 \\ 5 & 4808 & 547 \\ 38 & 547 & 4085 \end{pmatrix}$$

The tortuosity of S3 in the x-, y-, and z- directions varies in the range [1.39, 1.47] (Table 2), and the largest value is observed in the z-direction, which is in agreement with the lowest permeability in the z-direction.

5. Discussion

5.1. Validation of permeability by micro- and macro-scale rock descriptors

Each of the evaluated micro- and macro-scale rock descriptors supplies qualitative information about the sample permeability (Tables 2-3), which is used to validate the multi-methodological approach presented in this paper. Specifically, the increasing mercury effective saturation with increasing pressure shows a similar pore throat size distribution curve slope for sandstone samples S1 and S3 in the macro-pore throat range (Figure 7), suggesting that these samples have similar structural connectivity. However, S1 has a smaller volume fraction of pore space available for fluid flow that is controlled by macro pore throats (i.e., 81 % in S1 vs. 93 % in S3, Figure7) due to its higher contents of silt, clay, and Fe-ox cement. The intermediate layer (S2) with 19 % porosity comprises more fines, which form a clay matrix (Table 2) due to poor grain sorting and smaller mechanical resistance of clay to pressure under the burial conditions. Only ~15 % of the pore volume fraction in S2 is controlled by bottle-neck macro pore throats (Figure 7). However, the characteristic length of S2, 12.3 µm (Table 2), indicates that macro-pore connectivity is still possible even when the pore space consists mainly of sub-macro-scale porosity. This 0.15 volume fraction is in agreement with Harter (2005), who estimated a volume fraction threshold of 0.13 for correlated yet random 3D fields required for full interconnectivity.

The value of the connectivity index of S3 (10) is approximately three times higher than that of S1 (3.49), while both rocks are defined as moderately sorted sandstones (Table 2). This difference is due to S1 having a smaller number of inequivalent loops within the pore network than S3, leading to smaller β_1 values in Euler characteristics (see Supplementary material for more detail). Inequivalent loops are correlated with pore throats; their number is affected by the resolution of the CT image and by the partial volume effect at grain surfaces (Cnudde and Boone, 2013; Kerckhofs et al., 2008), where some voxels could be identified as grains and thus "clog" the small pore throats. Artefact porosity loss is apparent for S1, where the IP is 17.5 % (in contrast to the CT porosity of 23.5 % predicted from MIP, Table 2). The connectivity index of S2 (0.94, Table 2) is lower than those of both S1 and S3 because of the clay matrix, which clogs pores. The effect of the partial volume effect on the image connectivity and on the preservation of small features was reviewed by Schlüter et al. (2014).

A correlation was found between the grain size and the amount of Fe-ox cement in S1 evaluated at each slice along the z-direction (from the image analysis, Figure 20). Exceptionally large grains are detected (indicated by the red rectangle) near the cemented region at ~750 µm. Large grains and a relatively high amount of cement can also be observed in the S1 thin section (Figure 3b). Large grains cause large pores and generate relatively permeable horizons through which water flow and solute transport can become focused (McKay et al., 1995; Clavaud et al., 2008), supplying iron solutes. We suggest that a vadose zone was formed after flooding events, where the water flow mechanism could have changed from gravity dominated to capillary dominated. Water then flowed due to capillary forces along grain surfaces towards regions with larger surface areas, and iron solutes precipitated in a reaction with oxygen available in the partly saturated zone. We suggest that with time, this cementation mechanism caused a decrease in the pore throat size near the preferential path, while the preferential path with a low surface area remained open, eventually generating the observed anisotropic flow pattern.

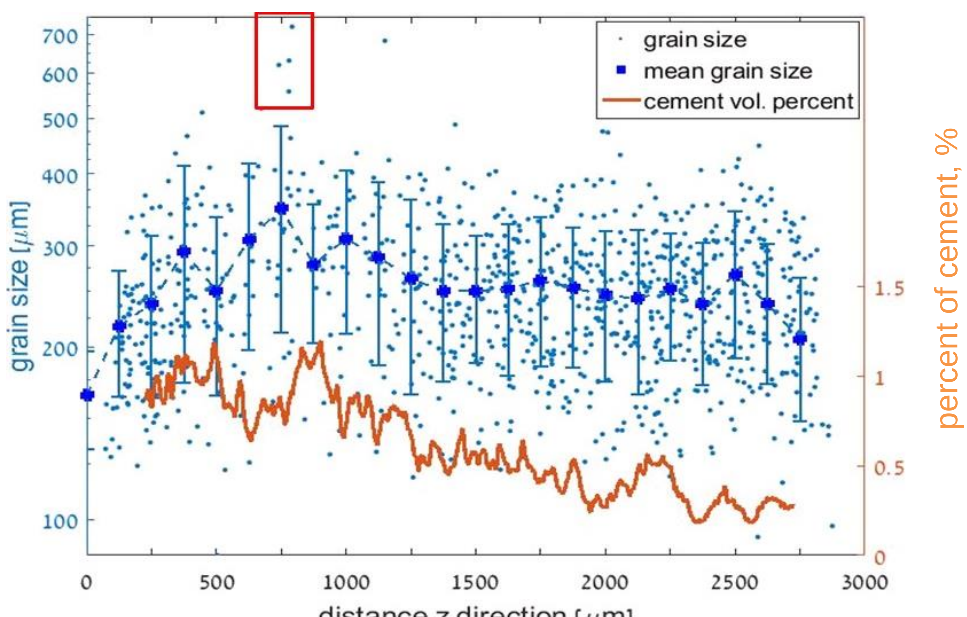

Figure 20. *Grain size scattering and Fe-ox cement content in sandstone S1 in slices along the z-direction.*

In this respect, permeability anisotropy in sandstones at a small scale is usually attributed to the shape or preferential orientation of grains and pores (e.g., Sato et al., 2019) and to a heterogeneous distribution of cementing material at grain contacts (Louis et al., 2005). At a larger scale, a higher degree of permeability anisotropy is associated with the presence of localized beds, foliation, and compaction bands that constitute barriers to flow in the perpendicular direction (see Halisch et al., 2009; Clavaud et al., 2008 and references therein). Clay-free and cement-free layers constitute the main avenues for flow in the parallel direction (e.g., Figure 12).

The semivariogram analysis of S1 reveals horizontal porosity bands with a thickness of ~1.6 mm (Figure 12c) that are composed of larger or smaller grains with larger or smaller pores between them, correspondingly. Flow modelling in the specified REV shows anisotropy (Table 2) and an average permeability value of 310 mD that is close to that derived from MIP (330 mD). However, the average permeability is lower than the average experimental gas permeability (~543 mD); this difference should be related to the loss of porosity due to limitations on the CT resolution, image processing and meshing (Table 3, see Sect. 5.2 for more details).

In contrast, no banding was detected in S3 by the semivariogram analysis (Figures 13-14). Flow modelling and upscaling to the macro scale indicate an isotropic sample (Table 2). However, the modelled permeability (~4500 mD) is ten times higher than the MIP-derived permeability (466 mD, Table 2). Gas permeability measurements indicate anisotropy, yielding permeabilities of 4600 mD in the x-y plane and 220 mD in the z-direction (with an anisotropy ratio of ~20, defined here as $\boldsymbol{\kappa}_{\parallel}/\boldsymbol{\kappa}_{\perp}$, e.g., Tiab and Donaldson, 2004). For comparison, the values of this ratio obtained from experimental permeability measurements were ~1.2 for Bentheim sandstone (Louis et al., 2005), ~1.7-2.5 for a sandstone within the Cretaceous Virgelle Member, Alberta, Canada (Meyer and Krause, 2001), and ~8.5 for Berea sandstone (Sato et al., 2019). However, in some laboratory measurements conducted parallel to the layering (in the x-y plane), poorly cemented grains in S3 could dislocate from the weakly consolidated sample due to the application of a pressure gradient. This could have resulted in a higher measured gas flux and thus a higher permeability parallel to the layering, yielding a high anisotropy. In this case, the permeability upscaled from the modelling in S3 is also exaggerated.

Alternatively, the disagreement between the laboratory-determined permeability (perpendicular to the layering) and the permeability obtained from the flow modelling (Table 2) may also stem from the small dimension of the modelled domain (cube edge length of ~0.875 mm), which may not have included the textural features that constrain fluid flow on a larger scale (e.g., Figure 5d). Nevertheless, additional permeability simulations on equivalently REV sized segmented sub-volumes of S3 and on the entire S3 have been conducted, to ensure consistency of the estimated REV size. These simulations have been performed by using the FlowDict module (Linden et al., 2015; 2018) of the GeoDict toolbox (Wiegmann, 2019) currently available at our disposal. Pre-processing as well as boundary conditions are identical to those used in COMSOL setup described in the Methods Sect. Sub-volumes locations, detailed permeability tensor simulation results as well as evaluated 3D image porosity data, can be found within the Appendix C. The permeability results are in a good agreement with previously conducted flow simulations (Table 2). The average permeability derived from all REV-sized sub-volumes is ~4381 mD, compared to the average permeability of ~4500 mD simulated upon the entire S3 geometry. This, again, is in a good accordance with the permeability of S3 measured parallel to the layering (Table 2). These simulations conducted in the sub-samples and in the full sample S3 (Appendix C), strengthen our conclusion that those may not have included the textural features that constrain fluid flow on a larger scale of the samples tested in the gas permeametry, Similarly, the differences with the permeability estimated by MIP seem to originate from the same reason.

For sample S2, both classic REV and semivariogram analyses indicated an REV size larger than the investigated sample size (Figure 18, Figs. B1 c,d in Appendix A). For this reason, the analytical programme formulated in our study cannot entirely be applied to S2 due to the impossibility of determining a reliable REV and hence conducting pore-scale flow modelling. As a result, although sample S2 represents a common sandstone, it is very heterogeneous in nature, and a sample larger than at least 9 mm (which is a maximal size of the tested domain) is required to capture its REV. The MIP-derived permeability is 4 mD; this low permeability is due to a clay-rich matrix that encloses substantial void space (Hurst and Nadeau, 1995; Neuzil, 2019). The gas permeability of the quartz wacke layer (S2, ~4.6 mD on average) is approximately two orders of magnitude lower than that of the quartz arenite layers (S1 and S3, Table 2). The permeability anisotropy ratio of S2 is ~2.8. The high inverse correlation between the porosity and clay matrix content enhanced in the z-direction (Figures 15c,16c) suggests that the clay matrix pattern appears as horizontal layering, thus generating the observed anisotropy.

Finally, non-marine sandstones of Lower Cretaceous age (as well as sandstones in general), feature a big complexity and variability in their characteristics, as immediately seen even from a comparison of our samples S1, S2, S3 from the same outcrop (Table 2). The distinctions usually stem from the different depositional and diagenetic conditions. For instance, low porosity of Wealden quartz arenite sandstones from Weald Basin within Ashdown and Wadhurst Clay Fms. in southeast England, ranges between 6.3 % and 13.2 %, while permeability between 0.4 mD and 11.9 mD (Akinlotan, 2016), suggested to be controlled mainly by grain sizes, grain shapes, and sorting that are directly linked to their depositional environment. Average porosities of 3.06 % and 0.19 % were evaluated in medium and fine grained tight gas sandstones, correspondingly, from Lower Cretaceous Denglouku Fm. in the Songliao Basin, China (Zhang et al., 2019). Alternatively, a secondary porosity of 4 % to 22 % was generated by acidic fluids acting in the compactional regime, destructing a high primary porosity in sandstone of Lower Cretaceous Shurijeh Fm. in the eastern Kopet-Dagh Basin in NE Iran (Moussavi-Harami and Brenner, 1993), while significant average porosity and permeability of 20 % and 3700 mD, respectively, were quantified in the Masila Block, Upper Qishn Fm. of the Lower Cretaceous Age, Republic of Yemen (Harding et al., 2002). Multi-methodological approach suggested in this study is applicable to all those sandstones with broad ranges of their textural, topological and mineralogical characteristics and should lead to their accurate petrophysical characterization.

5.2. Upscaling permeability: accuracy of the extended computational workflow

The extended computational workflow (Figure 2) serves as the main tool in this study for upscaling permeability from the pore-scale velocity field. The accuracy of each step in the workflow affects the ultimate result.

Following the steps of the workflow, a micro-CT image resolution of 2.5 μm limits the reliability of the representation of the porous medium and defines the lower pore identification limit using this method. As an example of this limitation, the *SSA* (bulk specific surface area) calculated by MIP is larger than the *PSA* (pore specific surface area) calculated by micro-CT image analysis in all the samples (Table 2), although the pore volume is always smaller than the bulk volume. The *PSA* from micro-CT is limited by the image resolution and therefore does not consider relatively small pores with large surfaces. The *PSA*s of S1 and S3 are similar, but the *SSA* (from MIP) of S1 is 20 times larger than that of S3 because S1 has a larger surface area at small pores created mainly by Fe-ox cement (compare Figure 3c-f for S1 to Figure 5c for S3). S2 shows a *PSA* twice as large as that of S1 due to the presence of clay and clay matrix with large surface areas.

Image processing and segmentation were applied in this study to recover the image geometry, which was blurred by noise or affected by the partial volume effect (see Sect. 3). Then, the loss of pore space due to the resolution limits was estimated in this study from the amount of mercury filling the pores with diameters equal to the resolution limit (Figure 7a). After segmentation, sample S1 had a segmented image porosity of 17.5 % and a CT predicted porosity of 23.5 % from MIP (Tables 2, 3). Therefore, the difference in porosities generated by the partial volume effect in the image processing scheme (e.g., Cnudde and Boone, 2013) is a significant component of error, especially for small structures, such as pores with a large surface area-to-volume ratio. In contrast, the image porosity of S3 after segmentation was 28.3 %, which is close to the porosity of 30.4 % estimated from MIP (Tables 2, 3). This is a result of the very small degree of cementation and the absence of Fe-ox flakes in the majority of the sample pores, leading to the small contribution of the partial volume effect. In comparison, a fine-grained and well-sorted Lower Cretaceous Fm. sandstone from Heletz Field (e.g., Figure 1a) (Tatomir et al., 2016) comprising clay and calcite had MIP and micro-CT porosities of 26.7 % and 20.9 %, respectively.

An additional source of inaccuracy is the use of a porosity-based REV for permeability approximations. Mostaghimi et al. (2013) showed that for CT images of sandpacks (homogenous samples), the porosity-based REV had an edge length of 0.5 mm, whereas the permeability-based REV was twice as large. Moreover, the porosity- and permeability-based REVs in images of bead packs derived by Zhang et al. (2000) had edge lengths of 1.71 and 2.57 mm, respectively. According to Mostaghimi et al. (2013), larger REV values for permeability rely on contributions from the tortuosity and connectivity of pore spaces, whereas the larger REV values of Zhang et al. (2000) may be related to the heterogeneity of the sample.

Additional simulations performed in S3 presented in Appendix C support this conclusion. Both porosity and permeability demonstrate a good agreement with those estimated with flow simulations in the REV presented in Table 2, thus confirming a representativeness of the estimated REV and a continuity of these characteristics over the chosen sample. However, the differences in porosity between the sub-samples and the full sample are smaller than the corresponding differences in permeability (Appendix C), as anticipated from a porosity-based REV derivation discussed above.

Further, textural bedding at ~1.6 mm scale dominates the porosity anisotropy in S1 (Figure 12c, evaluated by the semivariogram), and by ~3.5 mm average thickness of two adjacent more and less porous beddings together. To upscale to permeability reliably, the REV domain should be sufficiently large such that it is bounded from below by the scale of the textural bedding (i.e., an edge length > 3.5 mm) but should not be larger than necessary to optimize computational efficiency (while remaining within the same scale of heterogeneity, i.e., at the macro scale). As a result, a REV with an edge length of ~2950 μm (~1.5 times larger than the scale of textural bedding) was chosen in the current study in sample S1. For comparison, in other studies, the edge lengths of REVs in sandstones were 0.68 mm (Ovaysi and Piri, 2010), 0.8 mm (Mostaghimi et al., 2013), and 1.2 mm (Okabe and Oseto, 2006; Tatomir et al., 2016). The larger REV size in the current study found by the semivariogram (rather than by the classic isotropic approach) was due to the textural features revealed in the z-direction.

Another source of inaccuracy is the geometry used for the flow model. The geometry considered in this study included only the pore network connecting six faces of the REV cube. Other pore spaces in the REV disconnected from the main network were deleted (because all paths smaller than the resolution were prescribed as grain pixels due to the partial volume effect), thus resulting in the smaller effective size of the simulation domain. The image porosity of sample S1 was 17.5 %, whereas its connected porosity was estimated as 15.6 % (Table 3), while those of sample S3 were 28.3 % and 27.9 %, respectively.

Furthermore, the mesh was generated by taking a trade-off between the size of the mesh elements (4 elements in the smallest pore throat) and computational limits into account while coarsening the mesh elements towards the pore centre. The connectivity between pores with very fine pore throats that could not be replaced by mesh elements could be lost, resulting in the loss of those pores in the calculations. In sample S1, the porosity used in the simulation was approximately 50 % smaller than the porosity estimated by gas porosimetry (Tables 2, 3). In contrast, the porosity used in the simulations in S3 was mostly preserved, comprising ~84 % of that estimated in the laboratory.

For comparison, in the fine-grained sample of the Lower Cretaceous sandstone from Heletz Field in Israel (Figure 1a), which has grain size characteristics similar to those of S1 but with higher clay and additional calcite contents (Tatomir et al., 2016), the permeability upscaled from micro-CT flow modelling (conducted by the same simulation method as that in the current study) exceeded the gas permeability by a factor of ~6. This could be related either to the small REV for the flow model or to the reduction in the specific surface area by image processing and meshing (Mostaghimi et al., 2013) for the flow modelling.

Finally, the upscaling process from the flow modelling successfully predicted the permeability anisotropy ratio of ~ 2.3 in S1, as discussed above. For comparison, the permeability anisotropy ratio evaluated using micro-CT flow monitoring in clay-free sandstones (Clavaud et al., 2008) had a mean value of ~2.5 (ranging from ~1.7 to ~5.2), related to the presence of less permeable silty layers. This is consistent with the ratio estimated at the pore scale in Rothbach sandstone (~5) (Louis et al., 2005), attributed to lamination due to differences both in the characteristics of the solid phase (grain size and packing) and in the content of the Fe-ox.

In this study we used the semivariogram range of spatial correlation of porosity as a parameter to determine the REV from CT data (in addition to the classic method suggested by Bear, 2013). The spatial correlation of porosity relates to a distance that fluid travels without being constrained by grains, and therefore to permeability. Calibrating the range of correlation of porosity by modelling the semivariogram for different sub-volume sizes sheds light on the specimen heterogeneity at the different scales. This approach could be applied for a series of CT datasets, to determine the REV from the range of correlations and to compare to the REV of permeability. Quantifying the spatial variability of structures which occur at different sub-volume sizes, may link to generation of preferential flow paths and to determination of effective porosity (associated with mobile water fraction) that is available for transport.

6. Conclusions

This paper presents a detailed description and evaluation of a multi-methodological petrophysical approach for the comprehensive multiscale characterization of reservoir sandstones. The validation was performed on samples from three different consecutive layers of Lower Cretaceous sandstone in northern Israel. The following conclusions can be drawn:

1. The suggested methodology enables the identification of links between Darcy-scale permeability and an extensive set of geometrical, textural and topological rock descriptors, which are quantified at the pore scale by deterministic and statistical methods. Specifically, micro-scale geometrical rock descriptors (grain and pore size distributions, pore throat size, characteristic length, pore throat length of maximal conductance, specific surface area, and connectivity index)

and macro-scale petrophysical properties (porosity and tortuosity), along with quantified anisotropy and inhomogeneity, are used to predict the permeability of the studied layers.

2. Laboratory porosity and permeability measurements conducted on centimetre-scale samples show less variability for the quartz arenite (top and bottom) layers and more variability for the quartz wacke (intermediate) layer. The magnitudes of this variability in the samples are correlated with the dimensions of their representative volumes and anisotropy, both of which are evaluated within the micro-CT-imaged 3D pore geometry. This variability is associated with clay and cementation patterns in the layers and is quantified in this study with image and semivariogram analyses.
3. Two different correlation lengths of porosity variations are revealed in the top quartz arenite layer by statistical semivariogram analysis: fluctuations at ~100 μm are due to variability in grain and pore sizes, and those at ~1.6 mm are due to the occurrence of high- and low-porosity horizontal bands occluded by Fe-ox cementation. The latter millimetre-scale variability is found to control the macroscopic rock permeability measured in the laboratory. Bands of lower porosity could be generated by Fe-ox cementation in regions with higher surface areas adjacent to preferential fluid flow paths.
4. More heterogeneous pore structures were revealed in the quartz wacke sandstone of the intermediate layer. This heterogeneity resulted from a combination of severalspatial structures, each one with an internal irregularity: the pore size at the scale of ~50 μm, the distance between the pores at the scale of ~350 μm, and the larger-scale more porous “lense” structures originated at the presence of patchy clay deposition at the ~1-2 mm distance.
5. Quartz arenite sandstone of the bottom layer shows stationarity in the investigated domain and lower anisotropy characteristics than that of the top layer, due to less horizontal cement bands. Modelling of the experimental semivariograms indicates a scale of ~0.1 mm in all directions, associated with the average size of pore cross-section.
6. The macroscopic permeability upscaled from the pore-scale velocity field simulated by flow modelling in the micro-CT-scanned geometry of millimetre-scale sample shows agreement with laboratory petrophysical estimates obtained for centimetre-scale samples for the quartz arenite

layers. The anisotropy in both estimates correlates with the presence of millimetre-scale bedding, also recognized by the semivariogram analysis.

7. The multi-methodological petrophysical approach detailed and evaluated in this study is particularly applicable for the detection of anisotropy at various rock scales and for the identification of its origin. Moreover, this method allows the accurate petrophysical characterization of reservoir sandstones with broad ranges of textural and topological features.

Acknowledgements

This project was supported by fellowships from the Ministry of Energy, Israel, and the University of Haifa. The authors are grateful to Igor Bogdanov from the University of Pau for his continuing scientific support. Special thanks to Rudy Swennen and his group from KU Leuven for their contributions to the MIP, thin section preparation, microscopy and micro-CT image processing; to Veerle Cnudde and her group from Ghent University for teaching us the image processing techniques; to Kirill Gerke and Timofey Sizonenko from the Russian Academy of Sciences for providing their image processing code; to Uzi Saltzman from Engineering Geology and Rock Mechanics Company, Israel, for sending his detailed historic geological description of the study area; and to Or Bialik, Nimer Taha and Ovie Emmanuel Eruteya from the University of Haifa, Israel, for their assistance in the laboratory work.

Competing interests

The authors declare that they have no conflicts of interest.

Author contributions

PH and RK designed the study. PH developed codes for pore-scale modelling with contributions by RK and MH. BS advised the microscopy and led the geological interpretations. MH scanned the samples and contributed to the statistical analysis conducted by PH. NW led the laboratory measurements. All co-authors participated in the analysis of the results. PH wrote the text with contributions from all co-authors. All co-authors contributed to the discussion and approved the paper.

Supplementary Material & Data Availability

3-D µ-CT datasets are freely available at the open access data repository "PANGAEA" under the given doi: https://doi.pangaea.de/10.1594/PANGAEA.907552.

References

Abed, A. M.: Depositional environments of the early cretaceous Kurnub (Hatira) sandstones, North Jordan, Sedimentary Geology, 31(3-4), 267-279, **1982**.

Akinlotan, O.: Porosity and permeability of the English (Lower Cretaceous) sandstones, Proceedings of the Geologists' Association, 127, 681-690, **2016**.

Akinlotan, O.: Mineralogy and palaeoenvironments: the Weald Basin (Early Cretaceous), Southeast England, The Depositional Record, 3(2), 187-200, **2017**.

Akinlotan, O.: Multi-proxy approach to palaeoenvironmental modelling: the English Lower Cretaceous Weald Basin, Geol. J. 53, 316–335, **2018**.

Ambegaokar, V., Halperin, B. I., & Langer, J. S. (1971). Hopping conductivity in disordered systems. *Physical review B*, *4*(8), 2612.

American Petroleum Institute, API : Recommended Practices for Core Analysis, RP 40, second edition, **1998**.

Amireh, B. S.: Sedimentology and palaeogeography of the regressive-transgressive Kurnub Group (Early Cretaceous) of Jordan, Sedimentary Geology, 112(1-2), 69-88., **1997**.

Andrä, H., Combaret, N., Dvorkin, J., Glatt, E., Han, J., Kabel, M., Keehm. Y., Krzikalla, F., Lee, M., Madonna, C., Marsh, M., Mukerji, T., Saenger, E., Sain, R., Saxena, N., Ricker, S., Wiegmann, A., and Zhan, X.: Digital rock physics benchmarks-Part I: Imaging and segmentation, Computers & Geosciences, 50, 25-32, **2013a**.

Andrä, H., Combaret, N., Dvorkin, J., Glatt, E., Han, J., Kabel, M., Keehm. Y., Krzikalla, F., Lee, M., Madonna, C., Marsh, M., Mukerji, T., Saenger, E., Sain, R., Saxena, N., Ricker, S., Wiegmann, A., and Zhan, X.: Digital rock physics benchmarks-Part II: Computing effective properties, Computers & Geosciences, 50, 33-43, **2013b**.

Arns, J.Y., Sheppard, A.P., Arns, C.H., Knackstedt, M.A., Yelkhovsky, A., and Pinczewski, W.V.: Pore-level validation of representative pore networks obtained from micro-CT images. In: Proceedings of the annual symposium of the society of core analysis, SCA2007-A26, Calgary, Canada, **2007**.

Asakawa, S., Watanabe, T., Lyu, H., Funakawa, S. and Toyohara, H.: Mineralogical composition of tidal flat sediments in Japan, Soil Science and Plant Nutrition, 1-9, **2020**.

Avigad, D., Kolodner, K., McWilliams, M., Persing, H., and Weissbrod, T.: Origin of northern Gondwana Cambrian sandstone revealed by detrital zircon SHRIMP dating, Geology, 31(3), 227-230, **2003**.

Avigad, D., Sandler, A., Kolodner, K., Stern, R. J., McWilliams, M., Miller, N., and Beyth, M.: Mass-production of Cambro-Ordovician quartz-rich sandstone as a consequence of chemical weathering of Pan-African terranes: Environmental implications, Earth and Planetary Science Letters, 240(3-4), 818-826, **2005**.

Bear, J.: Dynamics of fluids in porous media. Courier Corporation, Courier Corporation, **2013**.

Blunt, M. J., Bijeljic, B., Dong, H., Gharbi, O., Iglauer, S., Mostaghimi, P., Paluszny, A., and Pentland, C.: Pore-scale imaging and modelling, Advances in Water Resources, 51, 197-216, **2013**.

Boek, E. S., and Venturoli, M.: Lattice-Boltzmann studies of fluid flow in porous media with realistic rock geometries, Computers & Mathematics with Applications, 59(7), 2305-2314, **2010**.

Bogdanov, I. I., Guerton, F., Kpahou, J., and Kamp, A. M.: Direct pore-scale modeling of two-phase flow through natural media, in: Proceedings of the 2011 COMSOL Conference in Stuttgart, **2011**.

Bogdanov, I. I., Kpahou, J., and Guerton, F.: Pore-scale single and two-phase transport in real porous medium, in: Proceedings of ECMOR XIII-13th European Conference on the Mathematics of Oil Recovery, September, **2012**.

Boudreau, B. P.: The diffusive tortuosity of fine-grained unlithified sediments, Geochimica et Cosmochimica Acta, 60(16), 3139-3142, **1996**.

Brabant, L., Vlassenbroeck, J., De Witte, Y., Cnudde, V., Boone, M. N., Dewanckele, J., and Van Hoorebeke, L.: Three-dimensional analysis of high-resolution X-ray computed tomography data with Morpho+, Microscopy and Microanalysis, 17(2), 252-263, **2011**.

Brunke, O., Brockdorf, K., Drews, S., Müller, B., Donath, T., Herzen, J., and Beckmann, F.: Comparison between X-ray tube based and synchrotron radiation based μCT, in: Developments in X-ray Tomography VI, edited by: Stock, S. R., San Diego: SPIE, 7078, **2008**.

Calvo, R., The diagenetic history of Heletz Formation and the timing of hydrocarbons accumulation in Heletz-Kokhav oil field. M.Sc. thesis, The Hebrew University of Jerusalem, 72 p. (in Hebrew, with English abstract), **1992**.

Calvo, R., Ayalon, A., Bein, A., and Sass, E.: Chemical and isotopic composition of diagenetic carbonate cements and its relation to hydrocarbon accumulation in the Heletz-Kokhav oil field (Israel), Journal of Geochemical Exploration, 108(1), 88-98, **2011**.

Carman, P. C.: Fluid flow through granular beds, Trans. Inst. Chem. Eng., 15, 150-166, **1937**.

Cerepi, A., Durand, C., and Brosse, E.: Pore microgeometry analysis in low-resistivity sandstone reservoirs, Journal of Petroleum Science and Engineering, 35(3-4), 205-232, **2002**.

Clavaud, J. B., Maineult, A., Zamora, M., Rasolofosaon, P., and Schlitter, C.: Permeability anisotropy and its relations with porous medium structure, Journal of Geophysical Research: Solid Earth, 113(B1), **2008**.

Cnudde, V., and Boone, M. N.: High-resolution X-ray computed tomography in geosciences: A review of the current technology and applications, Earth-Science Reviews, 123, 1-17, **2013**.

Cohen, A., and Boehm, S.: Lithofacies and environments of deposition of the Lower Cretaceous Helez & Telamim Formations, Geological Survey of Israel Report No. 5, **1983**.

Cohen, Z.: The geology of the Lower Cretaceous in Southern Coastal Plain, Ph.D. thesis, The Hebrew University of Jerusalem, 98 pp. (in Hebrew, with English abstract), **1971**.

Cressie, N.. Fitting variogram models by weighted least squares. *Journal of the international Association for mathematical Geology*, *17*(5), 563-586, **1985**.

Du, S., Pang, S., and Shi, Y.: Quantitative characterization on the microscopic pore heterogeneity of tight oil sandstone reservoir by considering both the resolution and representativeness, J. Pet. Sci. Eng., 169, 388–392, **2018**.

Dullien, F. A.: Porous media: fluid transport and pore structure, Academic press, **2012**.

Harter, T.: Finite-size scaling analysis of percolation in three-dimensional correlated binary Markov chain random fields, Physical Review E, 72(2), 026120, **2005**.

Farrel, N.J.C., Healy, D., and Taylor, C.W.: Anisotropy of permeability in faulted porous sandstones. Journal of Structural Geology 63, 50-67, **2014**.

Ferreira, N. N., Ferreira, E. P., Ramos, R. R., and Carvalho, I. S.: Palynological and sedimentary analysis of the Igarapé Ipiranga and Querru 1 outcrops of the Itapecuru Formation (Lower Cretaceous, Parnaíba Basin), Brazil, Journal of South American Earth Sciences, 66, 15-31, **2016**.

Folk, R. L., and Ward, W. C.: Brazos River bar [Texas]; a study in the significance of grain size parameters, Journal of Sedimentary Research, 27(1), 3-26, **1957**.

Gardosh, M. A., and Tannenbaum, E.: The petroleum systems of Israel, in: Petroleum systems of the Tethyan region: AAPG Memoir, edited by: Marlow, L., Kendall, C., and Yose, L., 106, 179-216, **2014**.

Garfunkel, Z.: The pre-quaternary geology in Israel, in: The zoogeography of Israel, edited by: Tchernov, E., and Yom-Tov, Y., Dr W. Junk Publishers, Dordrecht, Netherlands, 7-34, **1988**.

Garfunkel, Z.: History and paleogeography during the Pan-African orogen to stable platform transition: reappraisal of the evidence from the Elat area and the northern Arabian-Nubian Shield, Israel Journal of Earth Sciences, 48, 135-157, **1999**.

Giesche, H.: Mercury porosimetry: a general (practical) overview. Particle & particle systems characterization, 23(1), 9-19, **2006**.

Grader, P., and Reiss, Z.: On the Lower Cretaceous of the Heletz area, Geological Survey of Israel, Bull No. 16, 14 pp., **1958**.

Grader, P.: The geology of the Heletz oil field, Ph.D. thesis, The Hebrew University of Jerusalem, 81 pp. (in Hebrew, with English abstract), **1959**.

Gringarten, E., and Deutsch, C.V.: Teacher's aide semivariogram interpretation and modeling. Mathematical Geology, 33(4), 507-534, **2001**.

Guibert, R., Horgue, P., Debenest, G., and Quintard, M.: A comparison of various methods for the numerical evaluation of porous media permeability tensors from pore-scale geometry, Mathematical Geosciences, 48(3), 329-347, **2016**.

Haldorsen, H. H., and Lake, L. W.: A new approach to shale management in field-scale models, Society of Petroleum Engineers Journal, 24(04), 447-457, **1984**.

Halisch, M.: Application and assessment of the lattice boltzmann method for fluid flow modeling in porous rocks, PhD thesis, Technical University of Berlin, 182 pp., **2013a**.

Halisch, M.: The REV Challenge – estimating representative elementary volumes and porous rock inhomogeneity from high resolution micro-CT data sets, Society of Core Analysts (SCA) Proceedings, SCA2013-069, **2013b**.

Halisch, M., Weller, A., Debschütz, W., Sattler, C. D., and El-Sayed, A. M.: A complex core-log case study of an anisotropic sandstone, originating from Bahariya Formation, Abu Gharadig Basin, Egypt, Petrophysics, 50(06), **2009**.

Haoguang, W. E. I., Kun, M. A., Xiang'an, Y. U. E., and Xinxin, W. A. N. G.: The Relationship of Ultra-Low Permeability Sandstone Aspect Ratio With Porosity, Permeability, Advances in Petroleum Exploration and Development, 7(1), 7-12, **2014**.

Harding, T. G., Norris, B., and Smith, K.H.: Horizontal Water Disposal Well Performance in a High Porosity and Permeability Reservoir Conference: SPE International Thermal Operations and Heavy Oil Symposium and International Horizontal Well Technology Conference. SPE-18153-MS, https://doi.org/10.2118/79007-MS, **2002**.

Hurst, A., and Nadeau, P. H.: Clay microporosity in reservoir sandstones: an application of quantitative electron microscopy in petrophysical evaluation, AAPG bulletin, 79(4), 563-573, **1995**.

Iassonov, P., Gebrenegus, T., and Tuller, M.: Segmentation of X-ray computed tomography images of porous materials: A crucial step for characterization and quantitative analysis of pore structures, Water Resources Research, 45(9), **2009**.

Jackson, M. D., Muggeridge, A. H., Yoshida, S., and Johnson, H. D.: Upscaling permeability measurements within complex heterolithic tidal sandstones, Mathematical Geology, 35(5), 499-520, **2003**.

Kalaydjian, F.: Origin and quantification of coupling between relative permeabilities for two-phase flows in porous media, Transport in porous media, 5(3), 215-229, **1990**.

Kass, M., Witkin, A., and Terzopoulos, D.: Snakes: Active contour models, International Journal of Computer Vision, 1(4), 321-331, **1988**.

Katz, A. J., and Thompson, A. H.: Prediction of rock electrical conductivity from mercury injection measurements, Journal of Geophysical Research: Solid Earth, 92(B1), 599-607, **1987**.

Kerckhofs, G., Schrooten, J., Van Cleynenbreugel, T., Lomov, S. V., and Wevers, M.: Validation of x-ray micro-focus computed tomography as an imaging tool for porous structures, Review of Scientific Instruments, 79(1), 013711, **2008**.

Khan, F., Enzmann, F., and Kersten, M.: Multi-phase classification by a least-squares support vector machine approach in tomography images of geological samples, Solid Earth, 7(2), 481-492, **2016**.

Knackstedt, M., Jaime, P., Butcher, A.R., Botha, P.W.S.K., Middleton, J., and Sok, R.: Integrating reservoir characterization: 3D dynamic, petrophysical and geological description of reservoir facies. In: Proceedings of the SPE Asia Pacific oil and gas conference and exhibition, 18–20 October, 2010, Brisbane, Queensland, Australia, SPE 133981, **2010**.

Kolodner, K., Avigad, D., Ireland, T. R., and Garfunkel, Z.: Origin of Lower Cretaceous ('Nubian') sandstones of North-east Africa and Arabia from detrital zircon U-Pb SHRIMP dating, Sedimentology, 56(7), 2010-2023, **2009**.

Kozeny, J.: Uber kapillare leitung der wasser in boden, Royal Academy of Science, Vienna, Proceedings Class I, 136, 271-306, **1927**.

Krinsley, D. H., Pye, K., Boggs Jr, S., and Tovey, N. K.: Backscattered scanning electron microscopy and image analysis of sediments and sedimentary rocks. Cambridge University Press, **2005**.

Lenormand, R.: Sca2003-52: Interpretation of mercury injection curves to derive pore size distribution, in: Proceedings of 2003 International Symposium of SCA., **2003**.

Legland, D., Arganda-Carreras, I., Andrey, P.: MorphoLibJ: integrated library and plugins for mathematical morphology with ImageJ. *Bioinformatics*, *32*(22), 3532-3534, **2016.**

Li, Y., He, D., Chen, L., Mei, Q., Li, C., and Zhang, L.: Cretaceous sedimentary basins in Sichuan, SW China: Restoration of tectonic and depositional environments, Cretaceous Research, 57, 50-65, **2016**.

Linden, S., Wiegmann, A., and Hagen, H.: The LIR space partitioning system applied to the Stokes equations, Graph. Models 82, 58–66 (2015).

Linden S., Cheng L., Wiegmann A.: Specialized methods for direct numerical simulations in porous media, Math2Market GmbH, technical report, https://doi.org/10.30423/report.m2m-2018-01. **2018**.

Liu, X., Wang, J., Ge, L., Hu, F., Li, C., Li, X., Yu, J., Xu, H., Lu, S., and Xue, Q.: Porescale characterization of tight sandstone in Yanchang Formation Ordos Basin China using micro-CT and SEM imaging from nm- to cm-scale, Fuel, 209, 254–264, **2017**.

Lewis, J.J.M.: Outcrop-derived quantitative models of permeability heterogeneity for genetically different sand bodies. In: SPE Annual Technical Conference and Exhibition, 2-5 October 1988, Houston, Texas, **1988**.

Louis, L., David, C., Metz, V., Robion, P., Menendez, B., and Kissel, C.: Microstructural control on the anisotropy of elastic and transport properties in undeformed sandstones. International journal of rock mechanics and mining sciences, 42(7-8), 911-923, **2005**.

Massaad, M.: Origin and environment of deposition of Lebanon basal sandstones, Eclogae Geologicae Helvetiae, 69(8), **1976**.

Mckay, G., Use of Adsorbents for the Removal of Pollutants from Wastewater. CRC press, **1995**.

MacKenzie, W. S., Adams, A. E., & Brodie, K. H. *Rocks and Minerals in Thin Section: A Colour Atlas*. CRC Press., **2017**.

Meyer, R., and Krause, F. F.: A comparison of plug-derived and probe-derived permeability in cross-bedded sandstones of the Virgelle Member, Alberta, Canada: The influence of flow directions on probe permeametry, AAPG bulletin, 85(3), 477-489, **2001**.

Meyer, R.: Anisotropy of Sandstone Permeability. CREWES Research Report, Vol. 14, 2002.

Mostaghimi, P., Blunt, M. J., and Bijeljic, B.: Computations of absolute permeability on micro-CT images, Mathematical Geosciences, 45(1), 103-125, **2013**.

Moussavi-Harami, R., and Brenner, R. L.: Diagenesis of non-marine petroleum reservoirs: the Neocomian (Lower Cretaceous) Shurijeh Formation, Kopet-Dagh basin, NE Iran. Journal of Petroleum Geology, 16(1), 55-72, **1993**.

Munawar, M.J., Lin, C., Cnudde, V., Bultreys, T., Dong, C., Zhang, X., De Boever, W., Zahid, M.A., and Wu, Y.: Petrographic characterization to build an accurate rock model using micro-CT: case study on low-permeable to tight turbidite sandstone from Eocene Shahejie Formation, Micron 109, 22–33, **2018**.

Narsilio, G. A., Buzzi, O., Fityus, S., Yun, T. S., and Smith, D. W.: Upscaling of Navier-Stokes equations in porous media: Theoretical, numerical and experimental approach, Computers and Geotechnics, 36(7), 1200-1206, **2009**.

Nelson, P. H.: Pore-throat sizes in sandstones, tight sandstones, and shales, AAPG bulletin, 93(3), 329-340, **2009**.

Neuzil, C. E.: Permeability of Clays and Shales, Annual Review of Earth and Planetary Sciences, 47, 247-273, **2019**.

Nordahl, K., and Ringrose, P. S.: Identifying the representative elementary volume for permeability in heterolithic deposits using numerical rock models, Mathematical Geosciences, 40(7), 753, **2008**.

Nordahl. K., Ringrose, P. S., and Wen, R.: Petrophysical characterisation of a heterolithic tidal reservoir interval using a process-based modelling tool, Petroleum Geoscience, 11, 17-28, **2005**.

Norris, R. J., and J. J. M. Lewis. The geological modeling of effective permeability in complex heterolithic facies, in SPE Annual Technical Conference and Exhibition, Society of Petroleum Engineers, **1991**.

Okabe, H., and Oseto, K.: Pore-scale heterogeneity assessed by the lattice-Boltzmann method, Society of Core Analysts (SCA2006-44), 12-16, **2006**.

Ovaysi, S., and Piri, M.: Direct pore-level modeling of incompressible fluid flow in porous media, Journal of Computational Physics, 229(19), 7456-7476, **2010**.

Pettijohn, F. J., Potter, P. E., and Siever, R.: Sand and Sandstone. Springer Verlag, 2nd ed., New York, **1987**.

Ploner, A.:The use of the variogram cloud in geostatistical modelling. *Environmetrics: The official journal of the International Environmetrics Society*, *10*(4), 413-437, **1999**.

Pyrcz, M. J., and Deutsch, C. V.: The whole story on the hole effect. Geostatistical Association of Australasia, Newsletter, 18, 3-5, **2003**.

Renard, P., Genty, A., and Stauffer, F.: Laboratory determination of the full permeability tensor, Journal of Geophysical Research: Solid Earth, 106(B11), 26443-26452, **2001**.

Reynolds, A. D.: Paralic reservoirs. Geological Society, London, Special Publications, 444(1), 7-34, **2017**.

Ringrose, P., and Bentley, M.: Reservoir Model Design: A Practitioner's Guide, Springer, 249 p. New York, **2015**.

Rootare, H. M., and Prenzlow, C. F.: Surface areas from mercury porosimeter measurements, The Journal of physical chemistry, 71(8), 2733-2736, **1967**.

RP40, A. P. I. (1960). API recommended practice for core-analysis procedure. *Edition, API, New York*, 12-13.

Rustad, A. B., Theting, T. G., and Held, R. J.: Pore space estimation, upscaling and uncertainty modelling for multiphase properties. In SPE Symposium on Improved Oil Recovery, Society of Petroleum Engineers, **2008**.

Saltzman, U.: Survey of the southeastern flanks of Mount Hermon, Tahal report (in Hebrew), **1968**.

Sato, M., Panaghi, K., Takada, N., and Takeda, M.: Effect of Bedding Planes on the Permeability and Diffusivity Anisotropies of Berea Sandstone, Transport in Porous Media, 127(3), 587-603, **2019**.

Schindelin, J., Arganda-Carreras, I., Frise, E., Kaynig, V., Longair, M., Pietzsch, T., Preibisch, S., Rueden, C., Saalfeld, S., Schmid, B., Tinevez, J., White, D., Hartenstein, V., Eliceiri, K., Tomancak, P., and Cardona, A.: Fiji: an open-source platform for biological-image analysis, Nature methods, 9(7), 676, **2012**.

Schlüter, S., Sheppard, A., Brown, K., and Wildenschild, D.: Image processing of multiphase images obtained via X-ray microtomography: a review, Water Resources Research, 50(4), 3615-3639, **2014**.

Schmitt, M., Halisch, M., Müller, C., and Fernandes, C. P.: Classification and quantification of pore shapes in sandstone reservoir rocks with 3-D X-ray micro-computed tomography, Solid Earth, 7(1), 285-300, **2016**.

Scholz, C., Wirner, F., Götz, J., Rüde, U., Schröder-Turk, G. E., Mecke, K., and Bechinger, C.: Permeability of porous materials determined from the Euler characteristic, Physical review letters, 109(26), 264504, **2012**.

Sethian, J. A.: A fast marching level set method for monotonically advancing fronts, Proceedings of the National Academy of Sciences, 93(4), 1591-1595, **1996**.

Shaw, S. M.: Southern Palestine geological map on a Scale 1:250,000 with explanatory notes, Palestine Geol. Soc. Publ., Jerusalem, **1947**.

Shenhav, H.: Lower Cretaceous sandstone reservoirs, Israel: petrography, porosity, permeability, AAPG Bulletin, 55(12), 2194-2224, **1971**.

Sheppard, A. P., Sok, R. M., and Averdunk, H.: Techniques for image enhancement and segmentation of tomographic images of porous materials, Physica A: Statistical mechanics and its applications, 339(1-2), 145-151, **2004**.

Shimron, A. E.: Tectonic evolution of the southern Mount Hermon, Geological Survey of Israel Report, GSI/10/98, **1998**.

Sneh, A., and Weinberger, R.: Geology of the Metula quadrangle, northern Israel: Implications for the offset along the Dead Sea Rift, Israel Journal of Earth Sciences, 52, **2003**.

Sneh, A., and Weinberger, R.: Metula sheet 2-11, Geology Survey of Israel, Ministry of Energy, **2014**.

Tatomir, A. B., Halisch, M., Duschl, F., Peche, A., Wiegand, B., Schaffer, M., Licha, T., Niemi, A., Bensabat, J., and Sauter, M.: An integrated core-based analysis for the characterization of flow, transport and mineralogical parameters of the Heletz pilot CO_2 storage site reservoir, International Journal of Greenhouse Gas Control, 48, 24-43, **2016**.

Stephens, D. B., Hsu, K. C., Prieksat, M. A., Ankeny, M. D., Blandford, N., Roth, T. Kelsey, J., Whitworth, J. R.: A comparison of estimated and calculated effective porosity. Hydrogeology Journal, 6(1), 156-165, **1998**.

Tiab, D., and Donaldson, E. C.: Petrophysics: Theory and Practice of Measuring Reservoir Rock and Fluid Transport Properties, Elsevier, **2004**.

Tidwell, V. C., and Wilson, J. L.: Permeability upscaling measured on a block of Berea Sandstone: Results and interpretation, Mathematical Geology, 31(7), 749-769, **1999**.

Vincent, L., and Soille, P.: Watersheds in digital spaces: an efficient algorithm based on immersion simulations, IEEE Transactions on Pattern Analysis & Machine Intelligence, 6, 583-598, **1991**.

Vogel, H. J.: Topological characterization of porous media, in: Morphology of condensed matter, edited by: Mecke, K. R., and Stoyan, D., Springer, Berlin, 75-92, **2002**.

Schwanghart, W.: Experimental (Semi-) Variogram (https://www.mathworks.com/matlabcentral/fileexchange/20355-experimental-semi-variogram), MATLAB Central File Exchange, **2020a**.

Schwanghart, W . variogramfit (https://www.mathworks.com/matlabcentral/fileexchange/25948-variogramfit), MATLAB Central File Exchange, **2020b**.

Wang, W. P., Liu, J. L., Zhang, J. B., Li, X. P., Cheng, Y. N., Xin, W. W., & Yan, Y. F. Evaluation of laser diffraction analysis of particle size distribution of typical soils in China and comparison with the Sieve-Pipette method. *Soil science*, *178*(4), 194-204, **2013**.

Viswanathan, J., Konwar, D., & Jagatheesan, K. Laboratory Characterization of Reservoir Rock and Fluids of Upper Assam Basin, India. In *Novel Issues on Unsaturated Soil Mechanics and Rock Engineering: Proceedings of the 2nd GeoMEast International Congress and Exhibition on Sustainable Civil Infrastructures, Egypt 2018–The Official International Congress of the Soil-Structure Interaction Group in Egypt (SSIGE)* (p. 179). Springer., **2018**.

Weissbrod, T.: Stratigraphy and correlation of the Lower Cretaceous exposures across the Dead Sea Transform with emphasis on tracing the Amir Formation in Jordan, Israel Journal of Earth Sciences, 51(2), 55–78, **2002**.

Weissbrod, T., and Nachmias, J.: Stratigraphic significance of heavy minerals in the late Precambrian-Mesozoic clastic sequence (“Nubian Sandstone”) in the Near East, Sedimentary Geology, 47(3-4), 263-291, **1986**.

Whitaker, S.: Flow in porous media I: A theoretical derivation of Darcy's law, Transport in porous media, 1(1), 3-25, **1986**.

Wiegmann, A.: GeoDict, the Digital Material Laboratory - Easy-to-use - Powerful - Accurate, Whitepaper, **2019**, https://doi.org/10.30423/WHITEPAPER.M2M-2019

Wildenschild, D., and Sheppard, A. P.: X-ray imaging and analysis techniques for quantifying pore-scale structure and processes in subsurface porous medium systems, Advances in Water Resources, 51, 217-246, **2013**.

Zhang, D., Zhang, R., Chen, S., and Soll, W. E.: Pore scale study of flow in porous media: Scale dependency, REV, and statistical REV, Geophysical research letters, 27(8), 1195-1198, **2000**.

Zhang, P., Leed,Y.I., and Zhange, J.: A review of high-resolution X-ray computed tomography applied to petroleum geology and a case study, Micron, 124, 102702, **2019**.

Zhu, W., Montési, L.G.J., and Wong, T.F.: Effects of Stress on the Anisotropic Development of Permeability during Mechanical Compaction of Porous Sandstones, Geological Society, London, 119-136, Special Publications, 200, **2002**.

Appendix A: Results of the REV determination by the classical approach

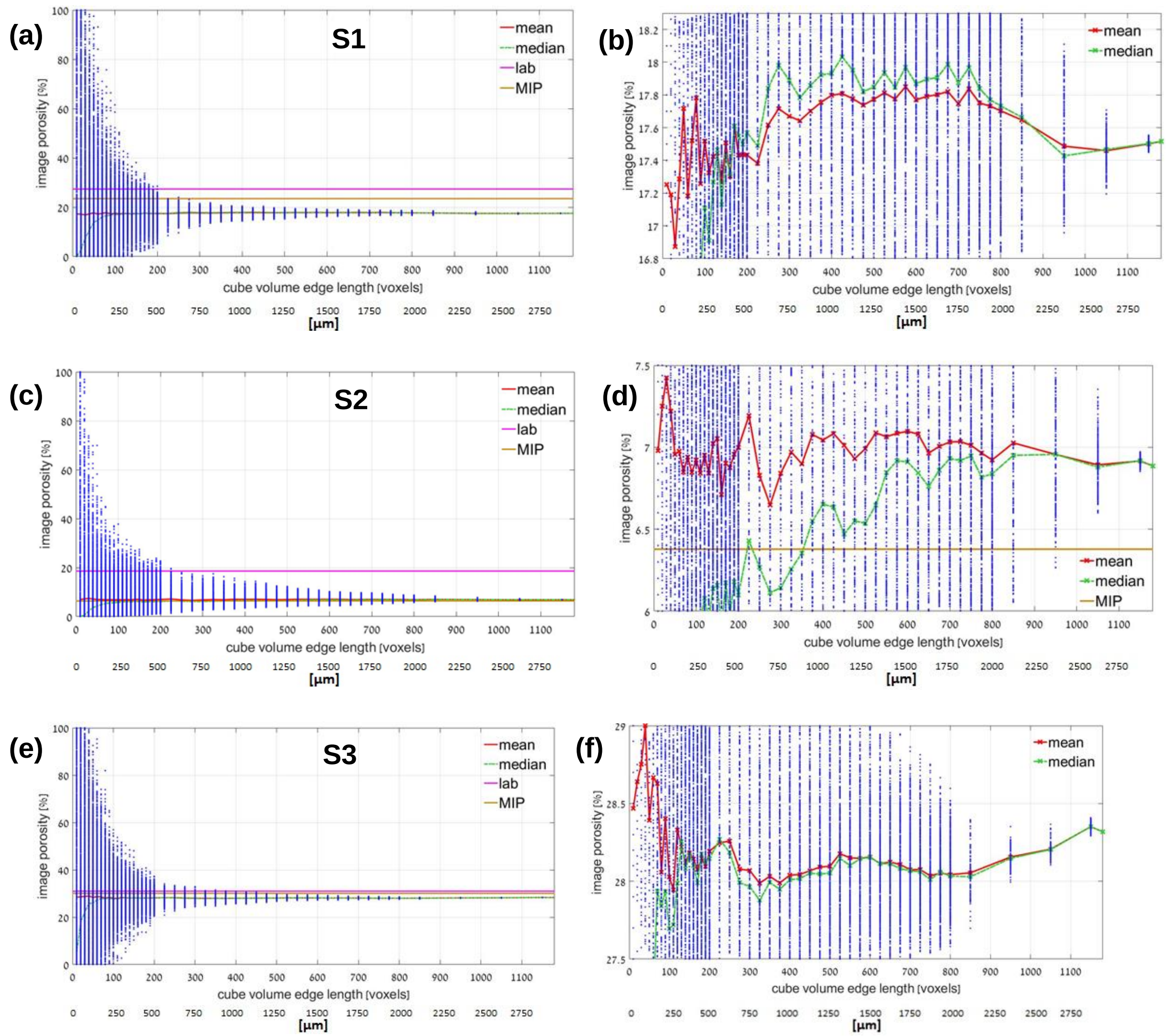

Figure A1: *Results of the classic REV analysis for sandstones S1-S3* ***(a,c,e)****.* ***(b, d, f)*** *Magnified views of the mean and median porosity trends of S1-S3 calculated for varying edge lengths. The scattering of porosity measured for each sub-volume is shown in blue dots. The laboratory porosities measured by gas porosimetry are shown by a pink line. The image porosity for CT, which was predicted by MIP for the resolution limit, is shown by a yellow line. The mean and median porosity are depicted by red and green lines, respectively.*

Appendix B: Maximum hydraulic conductance

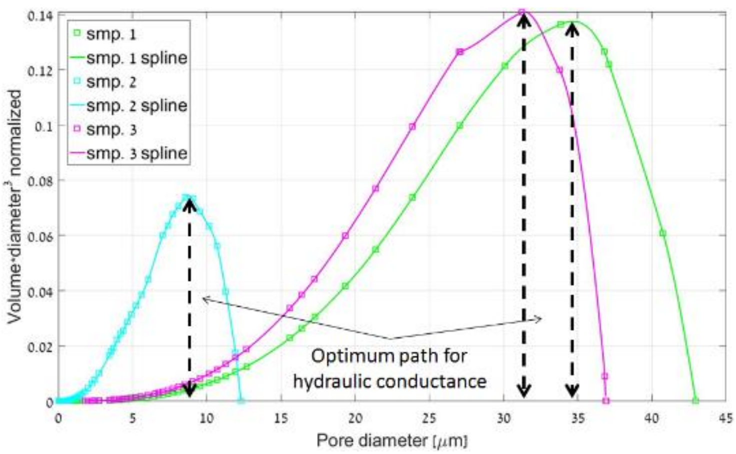

Figure B1: *The pore throat length of the maximal hydraulic conductance, l_{max}, is defined from the maximal (normalized) hydraulic conductance (Katz and Thompson, 1987), specified at the vertical axis of the chart. The corresponding pore throat diameters (x-axis) marked by black arrows define the pore throat diameters (or pore throat lengths of maximal conductance), l_{max}, where all connected paths composed of $l \geq l_{max}$ contribute significantly to the hydraulic conductance (see Sect.3.2).*

Appendix C: Setup and results of permeability tensor simulations in sub-samples using GeoDict (module FlowDict)

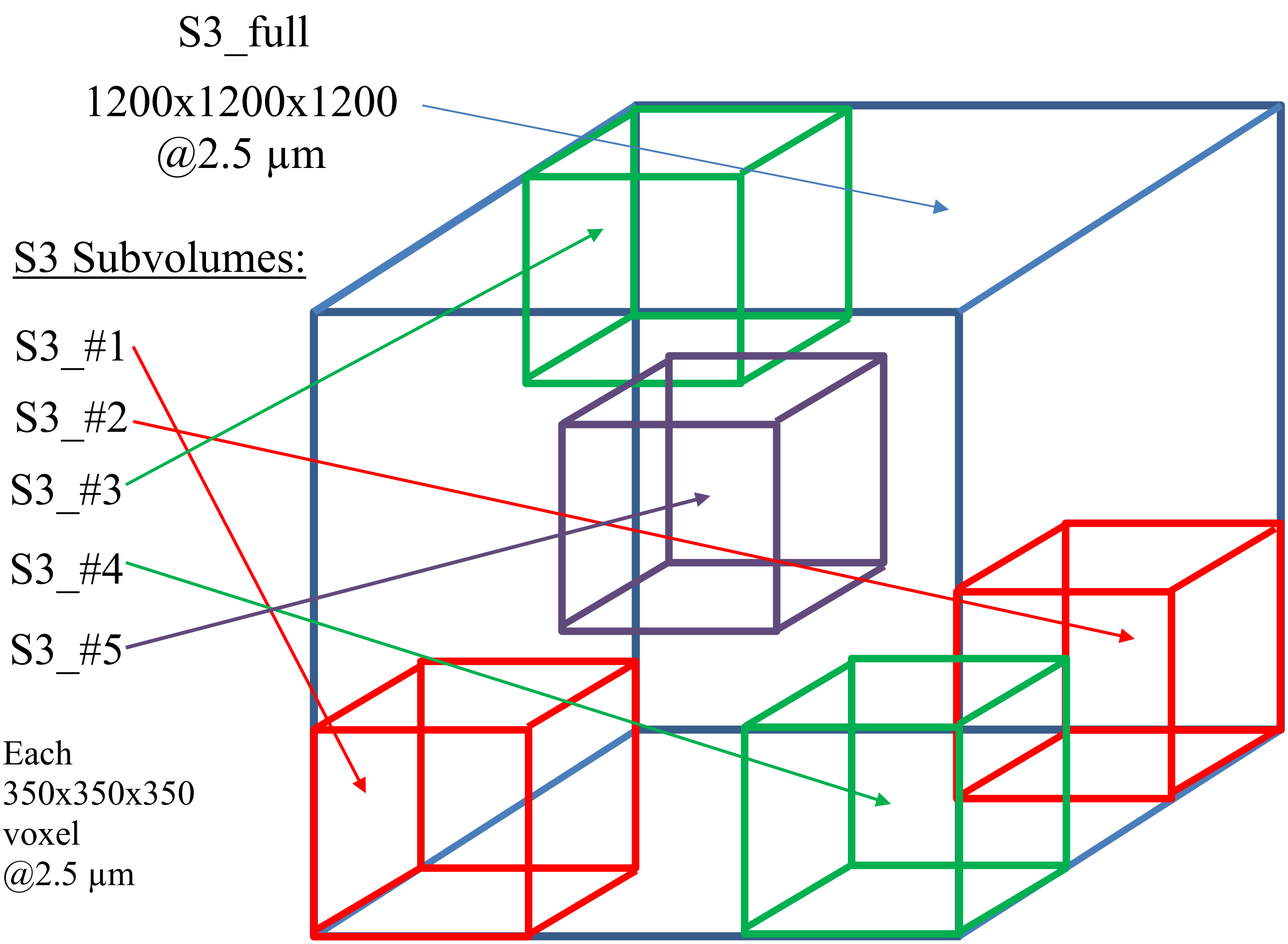

Figure C1: *Schematic of sub-volumes location in the full segmented sample of S3.*

S3_total

4247	98	116
98	4820	483
117	483	4432

avg. k: ~ 4500 mD
@ ϕ: 26.88 %

S3_#3

5032	9	10
1	4143	10
2	9	5223

avg. k: ~ 4799 mD
@ ϕ: 27.33 %

S3_#1

5485	119	3
130	5882	2
5	1	4504

avg. k: ~5290 mD
@ ϕ: 27.47 %

S3_#4

4601	2	3
6	3799	5
4	5	3344

avg. k: ~ 3915 mD
@ ϕ: 26.75 %

S3_#2

4392	179	68
75	3510	185
175	185	3359

avg. k: ~ 3754 mD
@ ϕ: 25.99 %

S3_#5

4397	9	68
10	3825	7
71	5	3858

avg. k: ~4027 mD
@ ϕ: 27.53 %

<u>In sub-samples:</u> avg. k: 4381 mD / median k: 4522 mD

Figure C2: *Results of permeability tensor simulations using GeoDict (module FlowDict).*